Aeolus 2.0's Thermal Rotating Shallow Water Model: A New Paradigm for Simulating Extreme Heatwaves, Westerly Jet Intensification, and More

Masoud Rostami[1,2], Stefan Petri[1], Bijan Fallah[3], and Farahnaz Fazel-Rastgar[4]

[1]Potsdam Institute for Climate Impact Research (PIK), Member of the Leibniz Association, Potsdam, Germany

[2]Laboratoire de Météorologie Dynamique (LMD) / IPSL, ENS-PSL Université, Ecole Polytechnique—Institut Polytechnique de Paris, Sorbonne Université, CNRS, Paris, France,

[3]Deutsches Klimarechenzentrum GmbH (DKRZ), Bundesstraße 45a, D-20146 Hamburg, Germany

[4]School of Chemistry and Physics, University of KwaZulu Natal, Durban 4000, SouthAfrica

1

Aeolus 2.0's Thermal Rotating Shallow Water Model: A New Paradigm for Simulating Extreme Heatwaves, Westerly Jet Intensification, and More

Masoud Rostami[1,2][⋆], Stefan Petri[1], Bijan Fallah[3], and Farahnaz Fazel-Rastgar[4]

[1]Potsdam Institute for Climate Impact Research (PIK), Member of the Leibniz Association, Potsdam, Germany
[2]Laboratoire de Météorologie Dynamique, Sorbonne University (SU)/ Ecole Normale Supérieure (ENS)/CNRS, 75005 Paris, France
[3]Deutsches Klimarechenzentrum GmbH (DKRZ), Bundesstraße 45a, D-20146 Hamburg, Germany
[4]School of Chemistry and Physics, University of KwaZulu Natal, Durban 4000, SouthAfrica

ABSTRACT

In this study, we demonstrate the dynamical core and applicability of Aeolus 2.0, a moist-convective Thermal Rotating Shallow Water (mcTRSW) model of intermediate complexity, along with its novel bulk aerodynamic and moist-convective schemes, in capturing the effects of increased radiative forcing on zonal winds and heatwaves. Simulations reveal seasonal patterns in zonal wind, temperature, and energy anomalies under increased radiative forcing during the summer solstice, winter solstice, and equinoxes. Increased radiative forcing enhances mid-latitudinal temperatures during the summer solstice in the Northern Hemisphere and the winter solstice in the Southern Hemisphere, leading to increased zonal wind velocity in the affected hemisphere, especially in the subtropics, while decreasing it in the opposite hemisphere. This thermal forcing also reduces the zonal wind velocity of polar cyclones in the hemisphere experiencing increased radiative forcing. During the autumn equinox, zonal wind velocity diminishes in the Southern Hemisphere, while a similar reduction occurs in the Northern Hemisphere during the spring equinox. Heightened meridional gradients significantly influence the poleward displacement of atmospheric circulation, particularly during the summer (northward) and winter (southward) solstices. Poleward eddy heat fluxes persist across hemispheres, indicating a consistent response to external heating. Increased radiative forcing during the summer and winter solstices amplifies prolonged heatwaves across land and ocean, exceeding impacts observed during the spring and autumn equinoxes.

⋆ Corresponding author: Masoud Rostami, Potsdam Institute for Climate Impact Research (PIK), Member of the Leibniz Association, P.O. Box 6012 03, D-14412 Potsdam Germany. E-mail: rostami@pik-potsdam.de, rostami@lmd.ipsl.fr

1 Introduction

The main goal of this study is to introduce the dynamical core of Aeolus 2.0 (Rostami et al., 2024a), an open-source atmospheric model of intermediate complexity developed by the Potsdam Institute for Climate Impact Research (PIK), and to demonstrate its applicability in capturing key aspects of large-scale atmospheric dynamics. Specifically, we highlight how Aeolus 2.0, which integrates the moist-convective Thermal Rotating Shallow Water (mcTRSW) model along with its novel bulk aerodynamic scheme, simulates atmospheric circulations driven by external forcing. As a case study, we investigate the impact of latitudinal temperature gradients - arising from midlatitude heating proportional to insolation - on seasonal variations in zonal wind patterns, particularly within the westerly jet stream.

The mcTRSW model builds on the tradition of the shallow water equations (SWEs), initially derived by Saint-Venant (Saint-Venant, 1871, 1888a,b). While SWEs were originally developed for studying water flows, their underlying mathematical framework has proven broadly applicable to geophysical fluid dynamics, including atmospheric and oceanic circulations. RSW models have been extensively studied and are widely used as a cost-effective and efficient tool for simulating a variety of natural flows. Their role in studying equatorial waves is well-supported, as shown by the foundational work of Matsuno (1966) and Gill (1980). The RSW model, which assumes fluid homogeneity, incompressibility, and hydrostatic balance, founded upon vertically averaged primitive equations utilizing pseudo-height as isobaric vertical coordinates (Zeitlin, 2018). The simplest RSW models represent barotropic processes in a single layer of incompressible fluid with a free surface, while multi-layer models are needed to capture baroclinic effects - those arising from the misalignment between density and pressure gradients (Pedlosky, 1987). However, a significant limitation of RSW models is their inability to accurately represent thermodynamic processes, which becomes particularly important for atmospheric layers where phenomena like moist convection and radiative transfer are prevalent. Notably, it tends to overlook the nuanced influence of horizontal gradients of potential temperature and moist convection, particularly in specific atmospheric and oceanic scenarios. Consequently, certain crucial atmospheric features, such as clouds, condensed liquid water content, and precipitable water, are inadequately represented

within the classical framework of the model. Unlike the classical configuration of RSW models, Thermal Rotating Shallow Water (TRSW) models introduce inhomogeneous layers, allowing horizontal variations in material properties within the RSW framework (Schopf and Cane, 1983; Ripa, 1993). This characteristic has prompted an alternative nomenclature for TRSW equations as the inhomogeneous-layer model in the scientific literature (Ripa, 1996). The conceptual framework of the TRSW model is firmly grounded in a robust theoretical foundation and has garnered substantial attention over the past few decades (Ripa, 1993, 1996; Warneford and Dellar, 2013; Holm et al., 2021; Rostami et al., 2022). This approach has been applied to investigate diverse phenomena, such as the dynamical effects of a well-mixed planetary boundary layer (Lavoie, 1972) and the formulation of a reduced two-dimensional system governing deep atmospheric motions under simple classes of stratification (Salby, 1989). In some instances, the TRSW model has been elucidated as a representation of an upper active layer of fluid atop a lower inert layer (Warneford and Dellar, 2013). With small adjustments to the model's parameters, the TRSW model could also be beneficial to the planetary sciences community. A notable advancement by Ripa (1993) reorganized a framework for a multi-layer thermal RSW model, coupled with a low-frequency approximation (Ripa, 1996). Ripa's studies demonstrated the Hamiltonian structure of TRSW models (see also Section C in the appendix). Hamiltonian dynamics provides a fundamental framework for classical mechanics, describing the evolution of systems in both finite and infinite dimensions. For finite-dimensional systems, this evolution is governed by Hamilton's equations: $\dot{q} = \partial H/\partial p, \quad \dot{p} = -\partial H/\partial q$, where q are the generalized coordinates, and p the conjugate momenta. The Hamiltonian $H(q, p)$ typically represents the total energy of the system, and these equations arise from the principle of least action. In the context of finite-dimensional systems, as described by Arnold (1978) and Landau and Lifshitz (1976), conserved quantities such as energy and momentum are tied to symmetries via Noether's theorem. In infinite-dimensional systems, such as those in fluid dynamics, the state variables are fields (e.g., velocity and pressure), and the Hamiltonian becomes a functional. The equations of motion are governed by generalized Poisson brackets, extending the finite-dimensional structure to handle infinitely many degrees of freedom (Arnold, 1978).

Recent contributions include Beron-Vera (2021), who derived another generalization of Ripa's single-layer model (Ripa, 1995) to an arbitrary number of layers with stratifi-

cation and shear. Kurganov et al. (2021) conducted a comparative analysis between the TRSW model and the isothermal RSW model, focusing on the dynamical processes of the evolution of isolated vortices in the mid-latitude β-plane, using a novel well-balanced central-upwind scheme. Additionally, Zerroukat and Allen (2015) presented a TRSW model derived from a three-dimensional Boussinesq approximation of the hydrostatic Euler equations, employing the absolute temperature as the thermodynamic variable.

Another feature of the TRSW model is that it is a layer model. Layer models and level models are two approaches used in ocean and atmosphere dynamics to represent the vertical structure of the atmosphere and oceans. In the RSW model, each layer represents the vertical integration of multiple levels, with the assumption that dynamical fields remain uniform in depth within each layer. As Ripa (1993) highlights, while level models can easily incorporate thermodynamics, they tend to be less accurate than layer models, particularly at high vertical modes. The difference lies in how these models represent the density profile. In a level model, density is assumed to be continuously stratified, and finite differencing is used at fixed depths. In contrast, a layer model approximates the continuous density profile with a piece-wise constant profile, where the depth of the interfaces can vary with position and time. Accuracy issues in level models arise from the inherent limitations of finite differencing at small scales. In contrast, layer models do not suffer from this problem because the piece-wise constant density profile is physically valid, and the equations of motion precisely represent this particular stratification (Ripa, 1993). The Laplace tidal equations (Proudman, 1942; Cartwright, 1978) serve as a prominent example that highlights the disparity between layer and level models. These equations, which describe the behavior of tides in the ocean and atmosphere, are a one-layer model with no counterpart in the level model family (Ripa, 1993).

It is worth mentioning that, to the best of our knowledge, despite the robust theoretical underpinnings highlighting the capabilities of the TRSW model, documented applications in contemporary scientific literature employing the TRSW modeling approach, specifically its integration as a dynamical core within atmospheric models and the practical implementation of multi-layer TRSW models on a spherical domain, have been sporadic and infrequent. This study aims to tackle and overcome this notable

6

limitation.

Aeolus 2.0 employs the Dedalus framework as a core component of its numerical methodology (Burns et al., 2020). That framework integrates the use of spin-weighted spherical harmonics, as detailed in the works of Vasil et al. (2019) and Lecoanet et al. (2019). A pivotal advantage of employing spin-weighted spherical harmonics in conjunction with spinor basis vectors lies in the ability to execute differentiation operations on the spherical domain in a manner analogous to Fourier series operations. This characteristic ensures that diagonal wavenumber multiplication remains regular across the entire sphere, thereby obviating the need for traditional singular gradients at the poles. This advantageous feature enhances the numerical stability and accuracy of calculations conducted within the TRSW model on a spherical domain. Aeolus 2.0 employs this enhanced mcTRSW framework to bridge the gap between simplified shallow water approaches and the complexity of three-dimensional general circulation models. This balance allows for computational efficiency while capturing essential physical processes

The modulation of the latitudinal temperature gradient and its subsequent impact on the amplitude of background zonal wind velocities and precipitation patterns represent fundamental components of atmospheric circulation, carrying significant implications for global meteorological and climatological systems (Petoukhov et al., 2013; Francis and Vavrus, 2015). As the westerly mean flows decrease due to a diminished meridional temperature gradient, jet streams exhibit increased wavier midlatitude jets (Moon et al., 2022), leading to the formation of quasi-stationary blocking high patterns. These atmospheric configurations contribute to the occurrence of severe flooding and drought events (Lupo, 2021). Despite research on the effects of latitudinal temperature gradients on zonal wind velocities (e.g. Francis and Skific, 2015; Mann et al., 2018; Moon et al., 2022), our understanding of how various forms of asymmetric thermal forcing in the northern and southern hemispheres across different seasons impact wind circulation remains limited. Indeed, the detailed dynamical mechanisms underlying these phenomena remain a topic of active debate.

2 Model description and setup of numerical experiments

2.1 The Multi-Layer Thermal Rotating Shallow Water (TRSW) Model

The model's dynamical core relies on a multi-layer pseudo-spectral TRSW model, complemented by an innovative approach to moist convection. Notably, this version of the TRSW model incorporates an improved moist-convective scheme, marking a refinement from the scheme introduced by Rostami et al. (2022). The conceptual framework of the model has already proven effective in simulating diverse atmospheric phenomena. For example, Rostami et al. (2022) proposed a theory elucidating the genesis and dynamics of the Madden Julian Oscillation. Additionally, it has been employed to simulate extreme localized heatwaves in midlatitudes (Rostami et al., 2024b).

Before describing the moist-convective scheme integrated into the model in this study, it is imperative to revisit the system of evolution equations governing a two-layer Thermal Rotating Shallow Water (TRSW) model within a "dry" framework. For the self-containment of this paper, we present the equations for the TRSW model. For a detailed derivation, the reader is referred to Rostami et al. (2022) and the appendices A and B of this paper.

$$(\partial_t + \boldsymbol{v}_1 \cdot \boldsymbol{\nabla})\boldsymbol{v}_1 + f\hat{\boldsymbol{z}} \times \boldsymbol{v}_1 = -\langle \boldsymbol{\nabla} p_1 \rangle, \tag{2.1a}$$

$$(\partial_t + \boldsymbol{v}_2 \cdot \boldsymbol{\nabla})\boldsymbol{v}_2 + f\hat{\boldsymbol{z}} \times \boldsymbol{v}_2 = -\langle \boldsymbol{\nabla} p_2 \rangle, \tag{2.1b}$$

$$\partial_t h_1 + \boldsymbol{\nabla} \cdot (h_1 \boldsymbol{v}_1) = 0, \tag{2.1c}$$

$$\partial_t h_2 + \boldsymbol{\nabla} \cdot (h_2 \boldsymbol{v}_2) = 0, \tag{2.1d}$$

$$\partial_t b_1 + \boldsymbol{v}_1 \cdot \boldsymbol{\nabla} b_1 = 0, \tag{2.1e}$$

$$\partial_t b_2 + \boldsymbol{v}_2 \cdot \boldsymbol{\nabla} b_2 = 0. \tag{2.1f}$$

The layer-averaged buoyancy variable, b_i, is defined as $g\bar{\theta}_i/\theta_s$, where θ_i is the vertically-averaged horizontal potential temperature in layer i, g is the acceleration due to gravity, and θ_s is the potential temperature at the lowermost layer, typically at the surface. The indices $i = 1, 2$ correspond to the lower and upper layers, respectively. $\boldsymbol{v}_i = (u_i, v_i)$ denotes the horizontal velocity, and $\langle \boldsymbol{\nabla} p_i \rangle = \boldsymbol{\nabla} \tilde{p}_i - \tilde{h}_i \boldsymbol{\nabla} b_i$ denotes the vertically-averaged

horizontal gradient of the pressure field. The parameter f presents the Coriolis parameter, while $\hat{\boldsymbol{z}}$ shows a unit vector in the vertical direction. Expressions for $\tilde{p}_1$, $\tilde{p}_2$, $\tilde{h}_1$, and $\tilde{h}_2$ are given by $\tilde{p}_1 = (h_b + h_1 + h_2)b_1$, $\tilde{p}_2 = h_1 b_1 + (h_b + h_2)b_2$, $\tilde{h}_1 = h_b + (1/2)h_1 + h_2$, and $\tilde{h}_2 = h_b + (1/2)h_2$. The variables h_1, h_2, and h_b represent the thicknesses of the lower layer, upper layer, and bottom topography, respectively. $\tilde{h}_1$ and $\tilde{h}_2$ physically express the center of mass of the corresponding layer. The quantities $\langle \boldsymbol{\nabla} p_1 \rangle$ and $\langle \boldsymbol{\nabla} p_2 \rangle$ can be expressed as $(1/2)h_1 \boldsymbol{\nabla} b_1 + b_1 \boldsymbol{\nabla}(h_b + h_1 + h_2)$ and $\boldsymbol{\nabla}(h_1 b_1) + (1/2)h_2 \boldsymbol{\nabla} b_2 + b_2 \boldsymbol{\nabla}(h_b + h_2)$, respectively. It is important to note that the vector fields of $\langle \boldsymbol{\nabla} p_i \rangle$ do not correspond to the gradient of a scalar. The derivation of the multi-layer TRSW model and its corresponding thermo-quasi-geostrophic (TQG) balance state can be found in Appendix A and B.

The two-layer mcTRSW model undergoes nondimensionalization using the barotropic equatorial Rossby deformation radius, denoted by, $L_d = (\sqrt{gH}/\beta)^{1/2}$, where $H = H_1 + H_2$ is the total non-perturbed layer depth, β denotes the gradient of the Coriolis force in the meridional direction. The scaling parameters for zonal and meridional velocities, temporal variables, and Earth radius (a) are defined as follows:

$$L \sim L_d, \quad (u, v) \sim \beta L_d^2, \quad t \sim \frac{1}{\beta L_d}, \quad a \sim L_d. \tag{2.2}$$

These evolution equations, governing the "dry" two-layer TRSW model, are valid within a defined horizontal domain $\mathscr{D}$. The first boundary condition is characterized by the absence of normal flux, expressed as:

$$\hat{n} \cdot h_i \boldsymbol{v}_i = 0, \quad \mathbf{x} \in \partial \mathscr{D}, \tag{2.3}$$

where $\hat{n}$ represents the outward unit vector and $\mathbf{x}$ represents a spatial coordinate or location within the defined horizontal domain $\mathscr{D}$.

An examination of the one-dimensional manifestation of the two-layer TRSW system, denoted as (2.1), reveals its conditional hyperbolic nature. Within the nonhyperbolic regime, the numerical solution of this system, as indicated by Cao et al. (2023), may exhibit instabilities. In the realm of practical applicability where $b_1 < b_2$, the hyperbolicity of the system (2.1) becomes contingent on the satisfaction of the inequality involving

the square of the velocity difference, denoted as $(v_1 - v_2)^2$:

$$(v_1 - v_2)^2 \leq \left(1 - \frac{b_1}{b_2}\right)(h_1 b_1 + h_2 b_2), \tag{2.4}$$

This condition serves as a critical determinant of hyperbolic behavior within the system. Specifically, when the magnitude of the velocity difference, represented as $|v_1 - v_2|$, is substantial, the system loses its hyperbolicity. This observation substantiates the previously mentioned association between the loss of hyperbolicity and the emergence of Kelvin-Helmholtz type instabilities.

In the realm of geophysical fluid dynamics, many models exhibit a Hamiltonian structure, a fundamental characteristic that imparts essential qualitative properties (Salmon, 1988). This structure establishes a direct link between symmetries and conservation laws through Noether's theorem, providing a deeper comprehension of the underlying dynamics (Shepherd, 1990). Additionally, it offers a framework for deriving nonlinear stability criteria using the energy-Casimir method (Holm et al., 1985; Morrison, 1998). Ripa (1993) demonstrated that a certain system of primitive equations models with inhomogeneous layers is Hamiltonian and introduced its Poisson bracket. The Hamiltonian structure of the reduced two-layer TRSW model, based on Ripa (1993), is revisited in Appendix C. A suitable Hamiltonian, which acts as a measure of the total energy in the system described by Equation (2.1), including both kinetic energy and gravitational potential energy, is defined as:

$$\mathscr{H} = \int_{\mathscr{D}} d^2 x \left[h_1 \left(\frac{1}{2} \boldsymbol{v}_1^2 + \tilde{h_1} b_1 \right) + h_2 \left(\frac{1}{2} \boldsymbol{v}_2^2 + \tilde{h_2} b_2 \right) \right]. \tag{2.5}$$

2.2   The improved moist-convective scheme of the TRSW Model

The moist-convective scheme used in the TRSW model, known as mcTRSW, builds upon the theoretical foundation of the moist-convective Rotating Shallow Water (mcRSW) model. The mcRSW model accounts for phase transitions of water vapor and latent heat release. Over time, the mcRSW model has undergone several improvements, including the integration of features such as precipitable water, vaporization, and precipitation (Bouchut et al., 2009; Lambaerts et al., 2011a,b, 2012; Rostami and Zeitlin, 2018). This scheme has been extensively applied to study the impacts of moist convection on the

dynamics of Earth's atmosphere (Lambaerts et al., 2012; Lahaye and Zeitlin, 2016; Rostami et al., 2017; Rostami and Zeitlin, 2019a,b, 2020, 2021, 2022; Zhao et al., 2021) as well as planetary atmospheres (Rostami et al., 2017, 2018). Based on previous work, the approach integrates the Lagrangian conservation of linearized equivalent potential temperature, incorporating convective fluxes and external thermal forcing. A hypothesis posits the change in horizontally averaged potential temperature and layer thickness, relating it to convective heating/cooling and external thermal forcing. Parameterization of condensed liquid water content and the inclusion of relaxation processes ensure closure within the model. In a two-layer representation, equations for layer thickness, buoyancy, humidity, and their Lagrangian derivatives are derived. External forcings such as insolation and thermal cooling are incorporated, along with a relaxation parameterization mechanism for condensation. Precipitable water and its interaction with condensation and vaporization are also included in the model. A major distinction in the moist-convective parameterization within the mcTRSW model in this study, compared to Kurganov et al. (2020) and Rostami et al. (2022), is the inclusion of downdrafts and the cooling effect due to sea surface evaporation.

Building upon the work of Rostami et al. (2022), our approach begins by integrating the Lagrangian conservation of the linearized equivalent potential temperature (moist enthalpy) in the primitive equation of a pair of pseudo-height material surfaces, z_{i-1} and z_i.

$$\lim_{\epsilon \to 0} \int_{z_{i-1}+\epsilon}^{z_i-\epsilon} \left[\frac{d}{dt} \left(\theta_i + \frac{\mathcal{L}}{C_p} q_i \right) \right] dz = \lim_{\epsilon \to 0} \int_{z_{i-1}+\epsilon}^{z_i-\epsilon} \mathbb{F}_i dz, \tag{2.6}$$

where $d/dt(\dots) = \partial_t(\dots) + \boldsymbol{\mathcal{V}} \cdot \nabla(\dots)$ represents the 3D Lagrangian derivative, $\boldsymbol{\mathcal{V}} = (u, v, w)$ represents the 3D velocity field, θ_i denotes potential temperature, q_i denotes specific humidity, $\mathcal{L}$ is the specific heat of vaporization, C_p denotes the specific heat at constant pressure, and $\mathbb{F}_i$ is external thermal forcing. Considering the columnar bulk of humidity as $\lim_{\epsilon \to 0} \int_{z_{i-1}+\epsilon}^{z_i-\epsilon} (\mathcal{L}/C_p) q_i dz = \bar{q}_i$, we obtain:

$$\Delta_i(\bar{\theta}_i h_i) + \Delta_i \bar{q}_i - \left(\frac{\bar{q}_i}{h_i} + \bar{\theta}_i \right) \Delta h_i = \bar{\mathbb{F}}_i, \tag{2.7}$$

where $h_i = z_i - z_{i-1}$, $\Delta_i(\dots) = \partial/\partial t(\dots) + \nabla \cdot \boldsymbol{v}_i(\dots)$, $\lim_{\epsilon \to 0} \int_{z_{i-1}+\epsilon}^{z_i-\epsilon} \mathbb{F} = \bar{\mathbb{F}}_i$, $\boldsymbol{v}_i$ is the vertically averaged horizontal velocity in layer i, $\bar{\theta}_i h_i = \lim_{\epsilon \to 0} \int_{z_{i-1}+\epsilon}^{z_i-\epsilon} \theta_i dz$ denotes the vertically averaged horizontal potential temperature. Indeed, we attribute the values of dependent variables $\theta(z_i), \theta(z_{i-1}), q(z_i), q(z_{i-1})$ at the vertical boundaries to their aver-

age values inside the layer. Thus, we obtain $\lim_{\epsilon \to 0}[\theta(z_i - \epsilon) = \theta(z_{i-1} + \epsilon)] = \bar{\theta}_i$ and similarly $\lim_{\epsilon \to 0}[(\mathcal{L}/C_p)q(z_i - \epsilon) = (\mathcal{L}/C_p)q(z_{i-1} + \epsilon)] = \bar{q}_i/h_i$. Boundary values may vary depending on specific configurations, as there is inherent ambiguity in choosing values at the interface between layers. To maintain consistency with the one-layer mc-TRSW model, we set $\theta(z_1) = \bar{\theta}_1$. Alternatively, choosing the mean difference of averaged values at the interface (cf. Rostami and Zeitlin, 2018) leads to having the Stokes drag distributed on the right-hand side of the momentum equations for both layers. In this model, we explore the impact of dominant non-adiabatic processes and external forcing from insolation, utilizing minimal parameters for convective processes. Consequently, we incorporate latent heat release due to condensation, including precipitable water, and account for related downdrafts and cooling in deriving a simplified two-layer system with a rigid lid.

We postulate a hypothesis asserting that the product of horizontally averaged potential temperature and layer thickness, $\bar{\theta}_i h_i$, undergoes an increase associated with latent heat release due to condensation and any external forcing, as well as a decrease linked to cooling processes. This hypothesis is expressed mathematically as follows:

$$\Delta_i(\bar{\theta}_i h_i) = \gamma(\mathcal{C}_i - \mathcal{D}_i) + \gamma^{\mathbb{F}}\bar{\mathbb{F}}_i, \quad 0 < \gamma, \gamma^{\mathbb{F}} \leq 1, \tag{2.8}$$

where $\mathcal{C}_i$ denotes the condensed liquid water content (CLWC) at each layer. We parameterize CLWC using the Betts-Miller method (Betts and Miller, 1986). The term $\gamma(\mathcal{C}_i - \mathcal{D}_i)$ represents the impact of the balance between convective heating and cooling processes, while $\gamma^{\mathbb{F}}\bar{\mathbb{F}}_i$ incorporates the influence of horizontally averaged external thermal forcing ($\bar{\mathbb{F}}_i$) on the rate of change of $\bar{\theta}_i h_i$. Both γ and $\gamma^{\mathbb{F}}$ are positive. The parameters γ and $\gamma^{\mathbb{F}}$ regulate the strength of these convective and external thermal forcing processes. The incorporation of $\mathcal{C}_i$ or $\mathcal{D}_i$ as a multi-functional variable plays a multifaceted role on the right-hand side of each equation corresponding to each layer, offering a physical interpretation for the hypothesis. They can be interpreted as either *adiabatic convective* processes, such as upward or downward convective fluxes across material surfaces, or *diabatic nonconvective* processes, such as cooling or warming, in the mcTRSW model. This allows the model to account for both mechanical and thermal effects of moist convection in most convection-coupled flows. Additional insights into the specific roles and interpretations of these variables will be further elaborated

upon in subsequent discussions.

In this two-layer model representation, condensation exclusively takes place in the lower layer ($\mathcal{C}_1 = \mathcal{C}, \mathcal{C}_2 = 0$). Consequently, in the lower layer, $\Delta_1(\bar{\theta}_1 h_1) = \gamma(\mathcal{C} - \mathcal{D}) + \gamma^{\mathbb{F}}\bar{\mathbb{F}}_1$, and $\Delta_1\bar{q}_1 = -\mathcal{C} + \mathcal{D}$. On the right-hand side (RHS) of $\Delta_1\bar{q}_1$, $\mathcal{C}$ functions as a sink for the columnar bulk of humidity in the lower layer, while $\mathcal{D}$ serves as a source. By assuming that $\Delta_1(\bar{\theta}_1 h_1) + \Delta_2(\bar{\theta}_2 h_2) = 0$, $\Delta_1\bar{q}_1 + \Delta_2\bar{q}_2 = 0$, substituting the corresponding values of $\Delta_i(\bar{\theta}_i h_i)$, $i = 1, 2$, and $\Delta_i\bar{q}_i$, $i = 1, 2$, in equation 2.7, and re-scaling $\bar{q}_i = (\mathcal{L}g/C_p\theta_s) \int q\, dz$ and $\bar{\mathbb{F}}_i = (g/\theta_s)\mathbb{F}_i$, $\bar{b}_i = g\bar{\theta}_i/\theta_s$, and dropping from now on the bars result in the following equations for a two-layer system:

$$\Delta_1 h_1 = \frac{1}{\epsilon_1 + b_1}\left[(1 - \gamma)(-\mathcal{C} + \mathcal{D}) - (1 - \gamma^{\mathbb{F}})\mathbb{F}_1\right], \tag{2.9a}$$

$$\frac{d_1 b_1}{dt} = \frac{1}{h_1}\left[\left(1 - \frac{\epsilon_1(1 - \gamma)}{\epsilon_1 + b_1}\right)(+\mathcal{C} - \mathcal{D}) + \left(\frac{\epsilon_1(\gamma^{\mathbb{F}} - 1)}{\epsilon_1 + b_1} + 1\right)\mathbb{F}_1\right], \tag{2.9b}$$

$$\Delta h_2 = \frac{1}{b_2 + \epsilon_2}\left[(1 - \gamma)(+\mathcal{C} - \mathcal{D}) - (1 - \gamma^{\mathbb{F}})\mathbb{F}_2\right], \tag{2.9c}$$

$$\frac{d_2 b_2}{dt} = \frac{1}{h_2}\left[\left(1 - \frac{\epsilon_2(1 - \gamma)}{\epsilon_2 + b_2}\right)(-\mathcal{C} + \mathcal{D}) + \left(\frac{\epsilon_2(\gamma^{\mathbb{F}} - 1)}{\epsilon_2 + b_2} + 1\right)\mathbb{F}_2\right], \tag{2.9d}$$

where $\epsilon_i = q_i/h_i$, $i = 1, 2$. In order to achieve closure within the system, condensation must be linked to the presence of moisture. This linkage is facilitated through a relaxation parameterization mechanism, wherein the moisture content relaxes with a characteristic time scale denoted by τ_c toward the saturation value Q^s, should the threshold be surpassed. Mathematically, this process is expressed as:

$$\mathcal{C} = \frac{q_1 - Q_s}{\tau_c}\mathbb{H}(q_1 - Q^s). \tag{2.10}$$

Here, $\mathcal{C}$ represents the rate of condensation, q_1 denotes the actual moisture content, and Q_s signifies the saturation moisture value. The Heaviside step function $\mathbb{H}(q_1 - Q^s)$ ensures that condensation occurs only when the actual moisture content surpasses the saturation threshold. Assuming $\epsilon_i \ll b_i$ for $i = 1, 2$, the reduction of the atmospheric

primitive equations in the two-layer mcTRSW model can be expressed as:

$$(\partial_t + \boldsymbol{v}_1 \cdot \boldsymbol{\nabla}) \, \boldsymbol{v}_1 + f\hat{\boldsymbol{z}} \times \boldsymbol{v}_1 = -\langle \boldsymbol{\nabla} p_1 \rangle, \tag{2.11a}$$

$$(\partial_t + \boldsymbol{v}_2 \cdot \boldsymbol{\nabla}) \, \boldsymbol{v}_2 + f\hat{\boldsymbol{z}} \times \boldsymbol{v}_2 = -\langle \boldsymbol{\nabla} p_2 \rangle - \frac{1-\gamma}{b_2 h_2} (\boldsymbol{v}_2 - \boldsymbol{v}_1) \, (\mathcal{C} - \mathcal{D}), \tag{2.11b}$$

$$\partial_t h_1 + \boldsymbol{\nabla} \cdot (h_1 \boldsymbol{v}_1) \quad = \frac{1}{b_1} \left[(1-\gamma)(-\mathcal{C} + \mathcal{D}) - (1 - \gamma^{\mathbb{F}}) \, \mathbb{F}_1 \right], \tag{2.11c}$$

$$\partial_t h_2 + \boldsymbol{\nabla} \cdot (h_2 \boldsymbol{v}_2) \quad = \frac{1}{b_2} \left[(1-\gamma)(+\mathcal{C} - \mathcal{D}) - (1 - \gamma^{\mathbb{F}}) \, \mathbb{F}_2 \right], \tag{2.11d}$$

$$\partial_t b_1 + \boldsymbol{v}_1 \cdot \boldsymbol{\nabla} \, b_1 \quad = \frac{1}{h_1} \left[(+\mathcal{C} - \mu \mathcal{E}) + \mathbb{F}_1 \right], \tag{2.11e}$$

$$\partial_t b_2 + \boldsymbol{v}_2 \cdot \boldsymbol{\nabla} \, b_2 \quad = \frac{1}{h_2} \left[(-\mathcal{C} + \mathcal{D}) + \mathbb{F}_2 \right], \tag{2.11f}$$

$$\partial_t q_1 + \boldsymbol{\nabla} \cdot (q_1 \boldsymbol{v}_1) \quad = -\mathcal{C} + \mathcal{E}, \tag{2.11g}$$

$$\partial_t q_2 + \boldsymbol{\nabla} \cdot (q_2 \boldsymbol{v}_1) \quad = +\mathcal{C} - \mathcal{D}. \tag{2.11h}$$

Herein, the Lagrangian derivative, denoted by $\partial/\partial t + \boldsymbol{v}_i \cdot \boldsymbol{\nabla}$, encapsulates the temporal evolution of quantities along the trajectory of fluid parcels. Notably, the presence of convective mass flux engenders a Stokes drag, as delineated in Equation 2.11b, arising from the vertical averaging of the horizontal momentum equations in the context of convective vertical velocity across the material interface. The structural fidelity to the non-thermal mcRSW archetype is preserved, albeit with nuanced options for its inter-layer distribution, elaborated upon in Rostami and Zeitlin (2018). The terms $\pm (\mathcal{C} - \mathcal{D})$ featured on the right-hand side of equations 2.11 embody both adiabatic convective (Equations 2.11c and 2.11d) and the terms $(-\mathcal{C} + \mathcal{D})$, $(+\mathcal{C} - \mathcal{E})$ diabatic nonconvective (Equations 2.11e and 2.11f) influences exerted on each layer. In the adiabatic convective process, vertical air movements (convection) facilitate convective fluxes across material interfaces. During this process, upward motion ($\mathcal{C}$), akin to an updraft, or downward motion ($\mathcal{D}$), akin to a downdraft, undergoes minimal heat exchange with the surrounding environment, as evidenced by the terms on the right-hand side of equations governing h_1 and h_2. The coefficients γ modulate the magnitude of these convective fluxes. When γ is set to 1, external forcing and latent heat release from condensation augment the average potential temperature of the fluid layer, rather than expelling convective plumes through the upper boundary. This yields a fully diabatic nonconvective model, akin to conventional formulations (Warneford and Dellar, 2013). While the coefficients γ and

$\gamma^{\mathbb{F}}$ may differ across layers, for the sake of parsimony, we maintain their uniformity.

Our model incorporates two external forcings affecting $\mathbb{F}_i$. First, insolation and its associated radiative transfer are accounted for using the rapid radiative transfer model (RRTM) (Mlawer et al., 1997; Iacono et al., 2000). Second, a thermal Newtonian cooling term, $-(h_i b_i - H_i B_i)/\tau_r$, is included, where τ_r denotes the relaxation time, and H_i and B_i signify the thickness and buoyancy at the rest state, respectively. To mitigate small-scale convective instabilities and alleviate numerical oscillations and instabilities within the momentum, mass, and buoyancy equations, a Laplacian damping mechanism has been introduced into the model. This approach draws inspiration from the concept of artificial viscosity, as outlined by Von Neumann and Richtmyer (1950) and further developed by Mattsson and Rider (2015). In scenarios where condensation is confined solely to the lower layer, q_2 in Equation 2.11h behaves as a passive tracer. However, should the model initiate the entrainment of condensed water from the lower layer to the upper layer followed by vaporization, vaporized water may act as a source of humidity on the right-hand side of Equation 2.11h, as elucidated by Rostami and Zeitlin (2018). In the absence of $\mathcal{D}$, continuous depletion of thickness h_1 due to water vapor condensation occurs, accompanied by a persistent loss of energy through convective updrafts that transport mass and momentum out of the lower layer (Rostami and Zeitlin, 2017; Zhao et al., 2021). Consequently, the model's practical utility for extended simulations becomes compromised. In the atmosphere model Aeolus 2.0, utilizing the mcTRSW scheme, $\mathcal{D}$ can be parameterized to uniformly descend from the upper layer to the lower layer where condensation does not occur. Alternatively, a non-uniform parameterization can be adopted, where descent occurs in proximity to the convective region, aligning more closely with realistic scenarios. In either case, there exists equilibrium in vertical mass exchange, such as between convective updrafts associated with condensation and downdrafts in non-condensing regions over the entire area $\mathscr{D}$: $\int_{\mathscr{D}} \sigma \mathcal{C} \, d^2 x = \int_{\mathscr{D}} (1-\sigma)\mathcal{D} \, d^2 x$, where σ denotes the area coverage of condensation. Conversely, the diabatic nonconvective process depicted on the right-hand side of equations governing the Lagrangian derivative of buoyancy in the lower and upper layers (Equations 2.11e & 2.11f) illustrates scenarios where heat exchange with the surroundings occurs, yet vertical air movement between layers remains a secondary influence.

The symbol $\mathcal{E}$, appearing on the right-hand side of Equations 2.11g and 2.11e, denotes the exogenous moisture contribution to the lower atmospheric layer. This influx

of moisture is parameterized as Rostami et al. (2024a), where a novel formulation tailored to the bulk aerodynamic scheme accounts for variations in buoyancy and zonal wind within the lower stratum. Within our modeling framework, we establish an equivalence between the amplitude of $\mathcal{E}$, which acts as a cooling effect in the lower layer in Equation 2.11e, and the corresponding warming term $\mathcal{C}$, due to latent heat release. This equivalence is mathematically expressed as: $\mu \approx \int_{\mathscr{D}} \mathcal{C} \, d^2x / \int_{\mathscr{D}} \mathcal{E} \, d^2x$. Parametrization of the total humidity source due to sea surface evaporation, $\mathcal{E}$, in this 2mcTRSW model combines temperature-driven vaporization, $\hat{\mathcal{E}}_{\text{vap}}(T_1)$, where T_1 is the temperature in the lower layer, wind-induced vaporization, $\hat{\mathcal{E}}_{\text{vap}}(|u_1^n|)$, where u_1^n is the normalized zonal wind velocity, and free convection (Fr. Conv.):

$$\mathcal{E}_{\text{vap}}(T_1) \quad = \mathbb{H}(Q^s - q_1) \exp\left[\frac{-\Delta H_{\text{vap}}}{R_v}\left(\frac{1}{T_1^\alpha} - \frac{1}{T_0^\alpha}\right)\right], \tag{2.12a}$$

$$\mathcal{E}_{\text{vap}}(|u_1^n|) \quad = \mathbb{H}(Q^s - q_1) \exp\left(\frac{|u_1^n|^{\alpha_{1v}}}{\alpha_{2v}}\right), \tag{2.12b}$$

$$\text{Fr. Conv.} \quad = \mathbb{H}(Q^s - q_1) \, \mathcal{A}_F \, (Q^s - q_1), \quad \text{if}\,(|u_1^n| \ll 1 \text{ and } b_1 \ll b_1^{\text{max}}), \tag{2.12c}$$

$$\mathcal{E}(T_1, |\boldsymbol{u}_1^n|, q_1) = \mathbb{H}(Q^s - q_1) \left(\mathcal{A}_T \, \hat{\mathcal{E}}_{\text{vap}}(T_1) + \mathcal{A}_u \, \hat{\mathcal{E}}_{\text{vap}}(|u_1^n|) + \text{Fr. Conv.}\right), \tag{2.12d}$$

where $\mathcal{A}_T$ and $\mathcal{A}_u$ are adjustable coefficients, and ΔH_{vap} denotes the enthalpy change during vaporization, which may be temperature-dependent. T_0 is the reference temperature. The Heaviside step function $\mathbb{H}(Q^s - q_1)$ guarantees that vaporization takes place only when the actual moisture content is below the saturation limit. The Free Convection term becomes predominant when the other two forces are negligible or absent. The normalized wind-induced vaporization term is given by: $\hat{\mathcal{E}}_{\text{vap}}(|\boldsymbol{u}_1^n|) = \mathcal{E}_{\text{vap}}(|\boldsymbol{u}_1^n|)/\text{Max}[\mathcal{E}_{\text{vap}}(|\boldsymbol{u}_1^n|)]$, which represents the normalized value of water vapor pressure due to wind-induced work of zonal velocity in the lower layer, scaled relative to its maximum value. Similarly, $\hat{P}_{\text{vap}}(T_1)$ is normalized as: $\hat{\mathcal{E}}_{\text{vap}}(T_1) = \mathcal{E}_{\text{vap}}(T_1)/\text{Max}(\hat{\mathcal{E}}_{\text{vap}}(T_1))$. The scaling factor α is calibrated by aligning model outputs with observational data. In our numerical experiments, the optimal empirical fits were achieved with $\alpha < 1$, typically ranging between 0.6 and 0.7. The behavior of $\hat{\mathcal{E}}_{\text{vap}}(|u_1^n|)$ aligns closely with findings from laboratory studies (Wirangga et al., 2023) and field observations (Penman, 1948), highlighting an increased vaporization rate under stronger wind conditions. This effect is captured using empirically derived parameters, with $\alpha_{1v} = 1.2$ and $\alpha_{2v} = 0.7$, which have been adopted in the current model configuration.

Condensed water persists in the atmosphere in the form of clouds, and precipitation occurs only when water droplets reach a critical size. Precipitable water, represented by Equation 2.13, has been incorporated into the model as another advected quantity denoted by W:

$$\partial_t W_i + \boldsymbol{\nabla} \cdot (W_i \boldsymbol{v}_i) = +\mathcal{C}_i - V_i - \mathcal{P}. \tag{2.13}$$

This quantity includes a source term attributed to condensation and a sink term attributed to vaporization (V) for each layer. The precipitation sink, denoted by $\mathcal{P}$, incorporated into Equation 2.13. Such a sink can be introduced through a relaxation process with a relaxation time τ_p, contingent upon a critical bulk amount of precipitable water in the atmospheric column:

$$\mathcal{P} = \frac{W_1 - W_{cr}}{\tau_p} \mathbb{H}(W_1 - W_{cr}). \tag{2.14}$$

Here, $\mathcal{P}$ represents the rate of precipitation sinking, W_1 denotes the actual precipitable water content, and W_{cr} signifies the critical bulk amount of precipitable water. The Heaviside step function $\mathbb{H}(W_1 - W_{cr})$ ensures that precipitation sinking occurs only when the actual precipitable water content exceeds the critical threshold. Precipitable water in the dynamical core of the 2mcTRSW model exits the system and does not directly affect the basic variables u_i, v_i, h_i, or b_i. However, in the coupled version of the model, it can be reintroduced as a freshwater source or as a forcing term in the ocean component.

The schematic representation of a spin-weighted spherical harmonic transform for a set of shallow water equations and the corresponding nondimensionalization process have been elucidated in prior works (Rostami et al., 2022, 2024b). The specific parameter values utilized for the Aeolus 2.0 model in our simulations are publicly available in the ZENODO repository (https://doi.org/10.5281/zenodo.13899262).

Built on the Dedalus framework, Aeolus 2.0 is implemented in Python. The simulations in this study were conducted with a grid resolution of 768×384 cells and a numerical time step of approximately 5 minutes. At this resolution, the model achieves a simulation speed of approximately 22 model years per day, utilizing 128 CPU cores with MPI parallelism on a high-performance cluster. The cluster is equipped with AMD Epyc 9554 "Genoa" processors (128 cores per compute node, up to 3.75 GHz clock frequency) and 6 GB of DDR5 memory per core.

456 To explore the vorticity and potential vorticity dynamics in the mcTRSW model,
457 we begin by considering small perturbations in layer thickness, represented as $h_i = H(1 + \lambda \eta_i)$, where λ serves as a small parameter controlling the perturbation amplitude,
459 and η_i denotes the layer-specific thickness anomaly. Starting from equations 2.11c and
460 2.11d, we derive:

$$\lambda \left[\partial_t \eta_i + H \boldsymbol{\nabla} \cdot (\eta_i \boldsymbol{v}_i)\right] + H \boldsymbol{\nabla} \cdot \boldsymbol{v}_i = \frac{1}{b_i} \alpha_i, \quad i = 1, 2, \tag{2.15}$$

462 where $\alpha_1 = (1 - \gamma)(-\mathcal{C} + \mathcal{D}) - (1 - \gamma^{\mathbb{F}}) \mathbb{F}_1$ and $\alpha_2 = (1 - \gamma)(\mathcal{C} - \mathcal{D}) - (1 - \gamma^{\mathbb{F}}) \mathbb{F}_2$
463 represent source terms accounting for convective and diabatic effects in each layer. In
464 the asymptotic limit as $\lambda \to 0$, equation 2.15 simplifies to

$$\boldsymbol{\nabla} \cdot \boldsymbol{v}_i = \frac{1}{Hb_i} \alpha_i, \quad i = 1, 2. \tag{2.16}$$

466 It is important to note that small variations in h within the TRSW model do not
467 necessarily imply a weak pressure gradient regime. By taking the cross-differentiation
468 of the u and v components of the momentum equations 2.11a and 2.11b and neglecting
469 Stokes drag for simplicity, without additional assumptions or external forcing $\mathbb{F}_i$, we
470 derive the evolution equation for absolute vorticity, $\zeta_i + f$, where $\zeta_i = \partial_x v_i - \partial_y u_i$:

$$(\partial_t + \boldsymbol{v}_i \cdot \boldsymbol{\nabla})(\zeta_i + f) = \mathcal{J}\left(\tilde{h}_i, b_i\right) - \frac{1}{Hb_i}(\zeta_i + f)\alpha_i. \tag{2.17}$$

472 Applying characteristic scalings for the variables:

$$(u_i, v_i) \sim U = \sqrt{HB}, \quad (x, y) \sim L, \quad t \sim \frac{L}{U}, \quad b \sim B, \tag{2.18}$$

474 we obtain the nondimensional divergence equations, using rescaled variables $\boldsymbol{v}_i^*$ and b_i^*
475 as derived from equation 2.11c:

$$\boldsymbol{\nabla} \cdot \boldsymbol{v}_i^* = \frac{1}{b_i^*} \tilde{\alpha}_i, \tag{2.19}$$

where $\tilde{\alpha}_i = (L/HBU)\,\alpha_i$ are the nondimensional source terms. In parallel to equation 2.17, the evolution of nondimensional absolute vorticity is given by:

$$(\partial_{t^*} + \boldsymbol{v}_i^* \cdot \boldsymbol{\nabla}^*)(\zeta_i^* + f^*) = \mathcal{J}\left(\tilde{h}_i^{\;*}, b_i^*\right) - \frac{1}{b_i^*}(\zeta_i^* + f^*)\tilde{\alpha}_i, \qquad (2.20)$$

where * indicates nondimensional variables. From equation 2.17, the potential vorticity for each layer, $\mathbb{Q}_i$, can be expressed in both dimensional and nondimensional forms within the mcTRSW model as follows:

$$(\partial_t + \boldsymbol{v}_i \cdot \boldsymbol{\nabla})\mathbb{Q}_i = \frac{1}{h_i}\mathcal{J}(\tilde{h}_i, b_i) - \frac{1}{Hb_i}\mathbb{Q}_i\alpha_i, \quad i = 1, 2, \qquad (2.21)$$

$$(\partial_{t^*} + \boldsymbol{v}_i^* \cdot \boldsymbol{\nabla}^*)\mathbb{Q}_i^* = \frac{1}{h^*}\mathcal{J}(\tilde{h}_i^{\;*}, b_i^*) - \frac{1}{b_i^*}\mathbb{Q}_i^*\tilde{\alpha}_i, \quad i = 1, 2. \qquad (2.22)$$

These vorticity and potential vorticity equations suggest that regions with positive values of $\mathcal{C}$ in the lower layer contribute to intensified vorticity and potential vorticity, emphasizing the role of convective processes as a source in the vorticity dynamics, while downdrafts ($\mathcal{D}$) act as a sink within the mcTRSW model.

3   Results

In order to conduct a comprehensive evaluation of the impact of equatorial heating on seasonal variations, we have selected four temporal intervals that encapsulate pivotal astronomical events, delineating notable phases in the Earth's orbit around the Sun: the summer solstice, winter solstice, and two equinoxes corresponding to the months of March, June, September, and December. The model initialization comprises daily averaged velocity and potential temperature variables extracted from the inaugural day of each aforementioned month (refer to Figures 1 and 2).

In our numerical experiments, the increased external heating force is scaled proportionally to the net radiative flux, which is defined as the difference between incoming shortwave radiation and outgoing longwave radiation. This results in an overall buoyancy anomaly that increases by up to approximately $\approx 5\%$ (as shown in the upper panel of Figure 3). It is important to note that this imposed forcing enhances the potential temperature gradient towards the polar regions; however, it differs from the process of
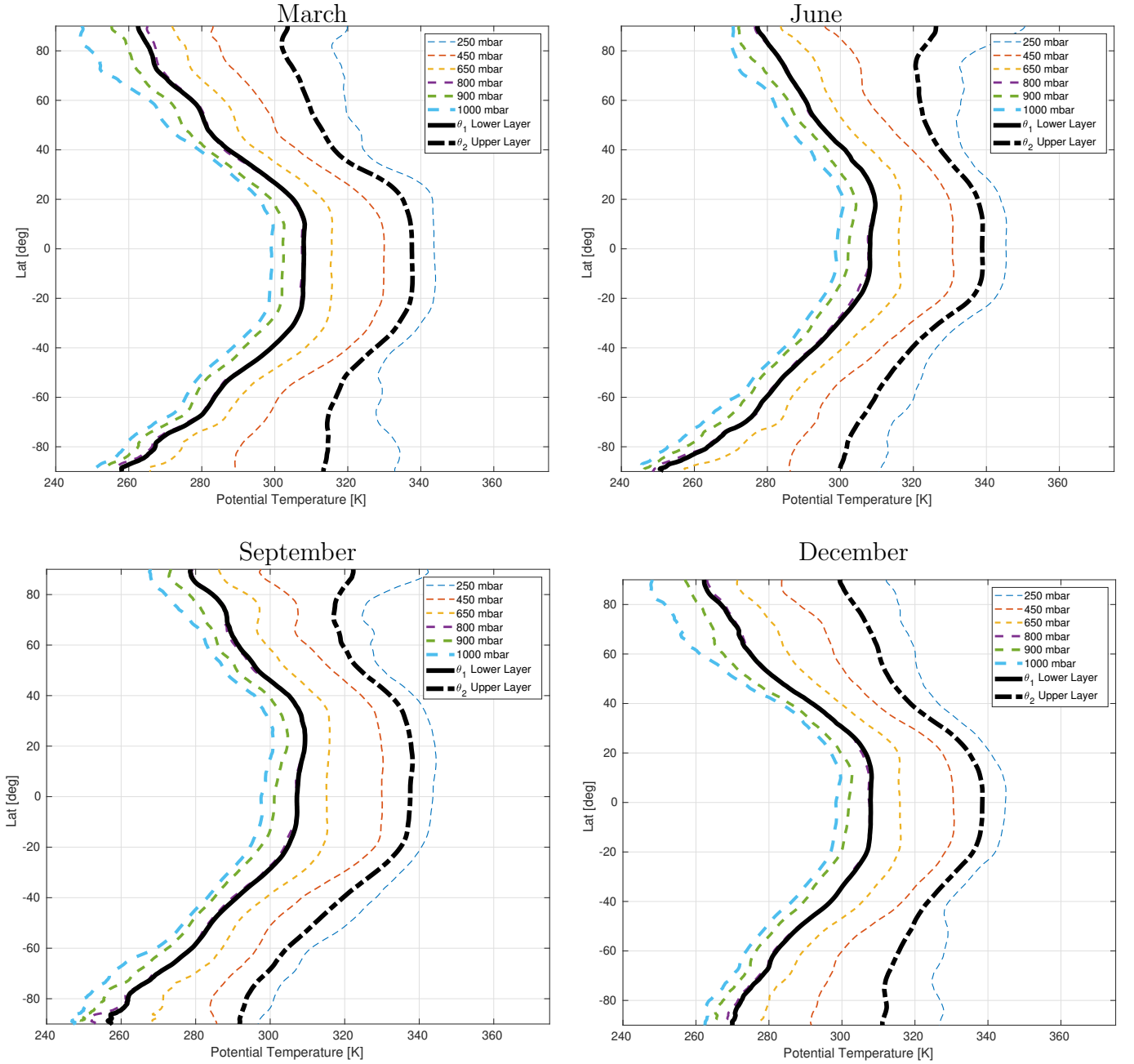
Figure 1. The zonally-averaged potential temperature distributions at different pressure levels are displayed for the initial days of March, June, September, and December in the year 1980. Thin dashed curves denote the ERA5 dataset. Meanwhile, thick black solid and dashed lines represent vertically integrated values for the lower and upper atmospheric layers, respectively, serving as input for the model. The upper layer encompasses levels at 450 mbar and 250 mbar, while the lower layer encompasses levels at 650 mbar, 800 mbar, 900 mbar, and 1000 mbar.

polar amplification. Polar amplification refers to a more pronounced warming at higher latitudes compared to lower latitudes, leading to a reduction in the meridional temperature gradient.

What is important about this type of forcing is that it directly modulates the net radiative flux rather than indirectly affecting temperature gradients through other climate feedback mechanisms. This approach allows for a more controlled and precise investigation of how changes in radiative flux can influence buoyancy and, consequently,
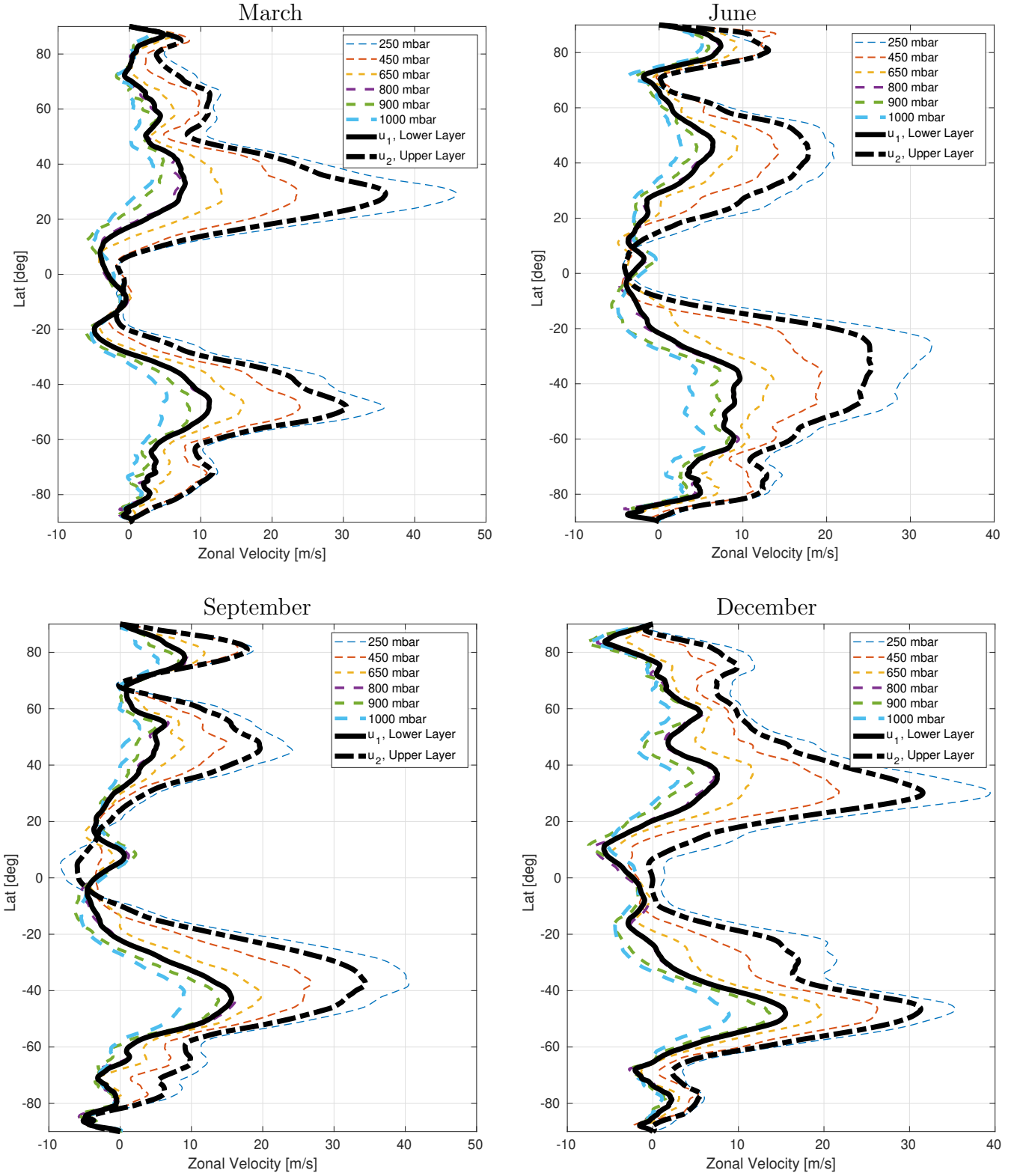
Figure 2. Zonal velocity averages at various pressure levels are showcased for the initial days of March, June, September, and December in the year 1980. The ERA5 data is depicted by thin dashed curves. Additionally, thick black solid and dashed lines illustrate the vertically integrated values for the lower and upper layers, respectively, serving as inputs to the model. The upper layer comprises levels at 450 mbar and 250 mbar, while the lower layer encompasses levels at 650 mbar, 800 mbar, 900 mbar, and 1000 mbar.

511 atmospheric circulation patterns. By isolating this variable, we can better understand

512 the specific contributions of radiative flux-driven heating to overall zonal wind dynamics.

513 As the peak external heating anomalies transition from the mid-latitudes of the North-
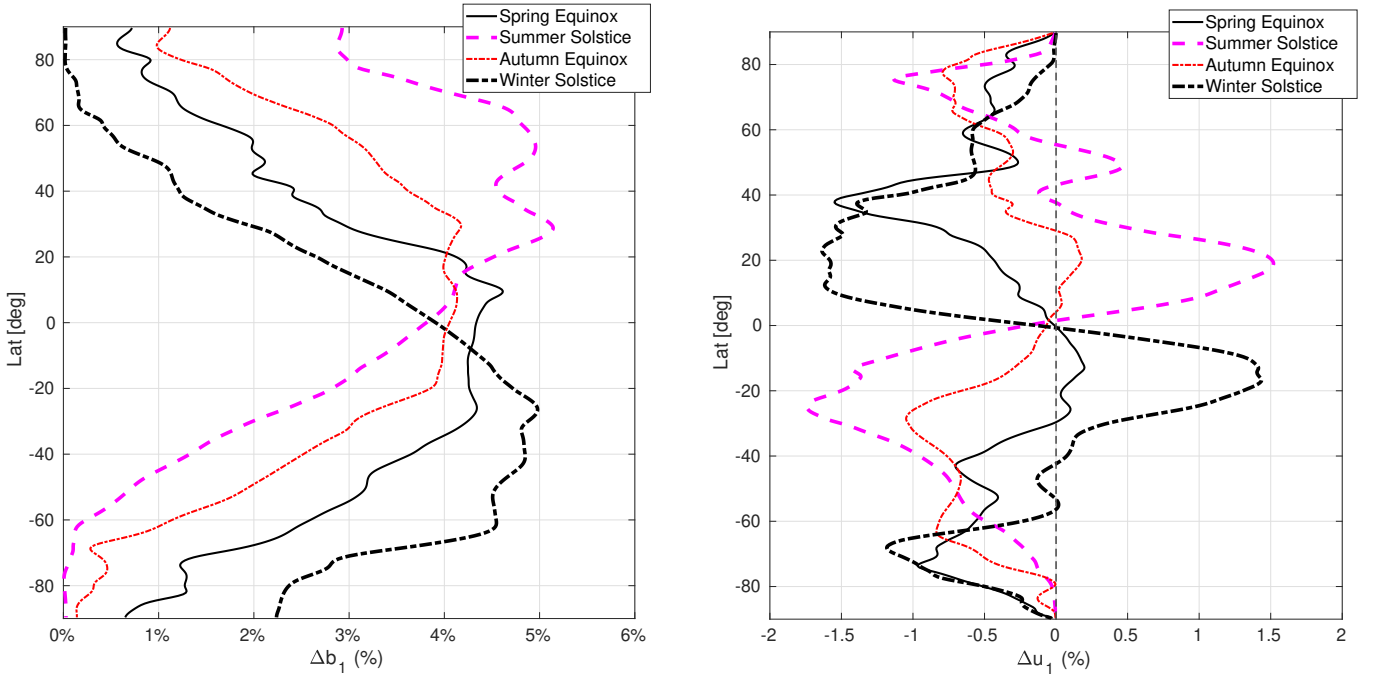
Figure 3. The left panel depicts the monthly averaged percentage increase in radiative forcing, which has impacted the buoyancy anomaly in the lower troposphere across four distinct seasonal periods: the spring equinox, summer solstice, autumn equinox, and winter solstice, relative to the initial conditions outlined in Figure 1. The x-axis represents the normalized buoyancy anomalies as percentages of the maximum unforced values, showcasing the variation in external heating forcing across different latitudes. The right panel portrays the resultant impact of these forcings on the zonal wind anomaly. The x-axis denotes the zonal wind anomaly normalized as a percentage of the maximum unforced zonal velocity.
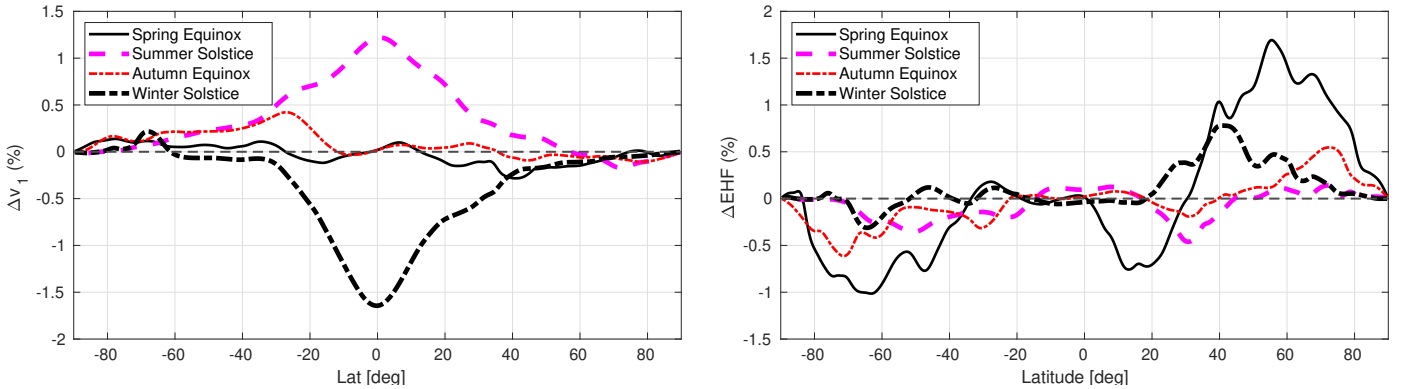

Figure 4. The left panel depicts the variation in the meridional velocity v_1 before and after the application of external heating forcing, while the right panel shows the variation in the lower layer's eddy heat flux (EHF) under the same conditions. Both panels present data averaged over all longitudes and illustrate changes for four distinct seasonal periods: the spring equinox, summer solstice, autumn equinox, and winter solstice. The y-axis represents the normalized anomaly as a percentage of the maximum unforced values, and the x-axis denotes the latitude in degrees. The results indicate how external heating forcing affects the meridional velocity and eddy heat flux across different latitudes during various seasons.

⁵¹⁴ ern Hemisphere (NH) to those of the Southern Hemisphere (SH), corresponding to the

⁵¹⁵ periods of the Summer solstice, autumn equinox, spring equinox, and winter solstice,

⁵¹⁶ there is a concurrent migration of zonal wind anomalies from the NH to the SH. Notably,

⁵¹⁷ across all the aforementioned forcing scenarios, a consistent observation emerges: the

⁵¹⁸ maximum zonal wind velocity manifests in the subtropical regions, specifically within

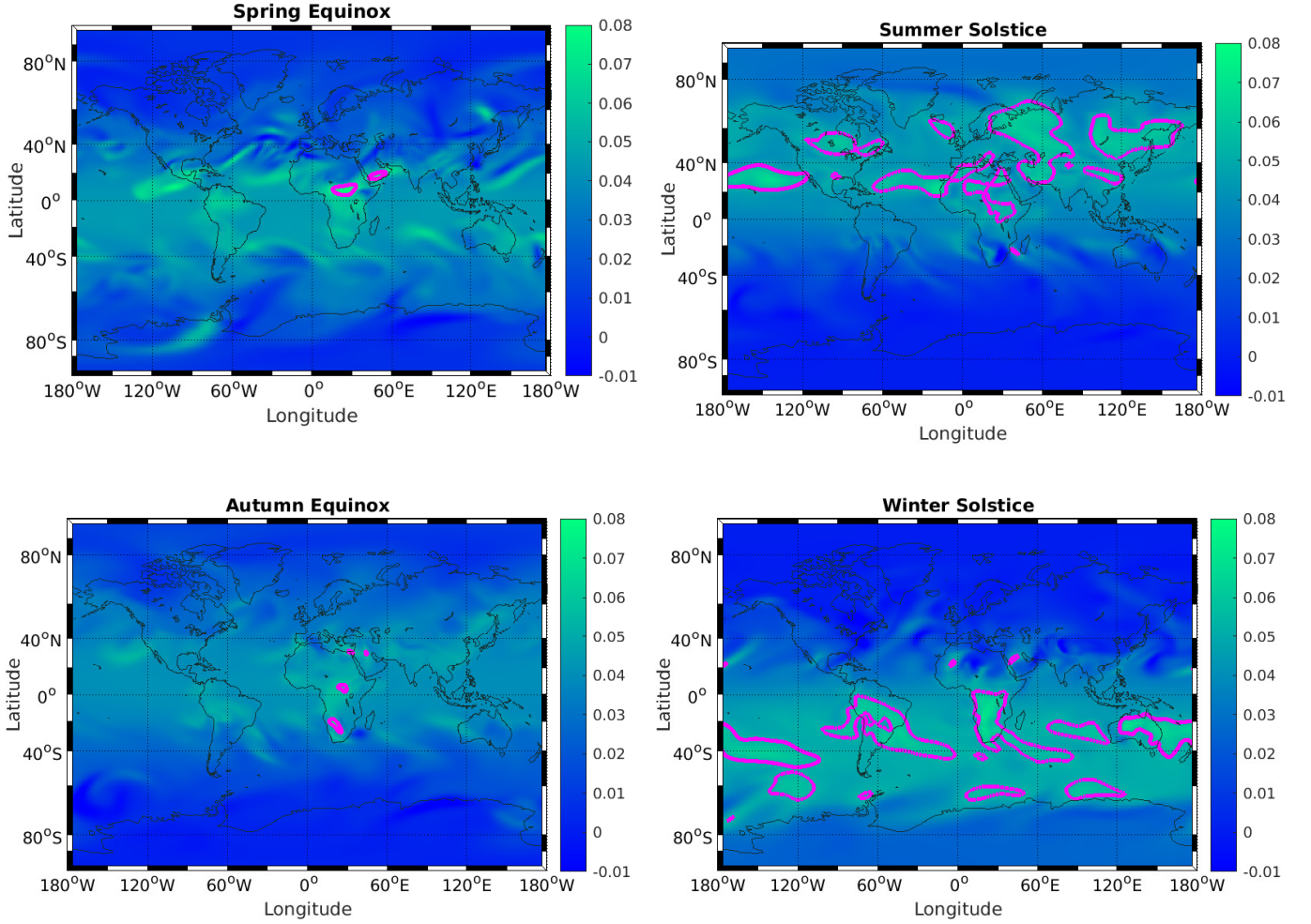⁵¹⁹ latitudes ranging from -20 to 20 degrees (Figure 3).

Figure 5. The figure illustrates a spatial distribution comparison of total buoyancy anomalies across four distinct seasonal periods: the Spring Equinox, Summer Solstice, Autumn Equinox, and Winter Solstice. This analysis captures buoyancy perturbations attributed to external heating influences. Thick magenta contour lines highlight regions with buoyancy anomalies greater than 75% of the maximum value observed under unforced conditions for each respective month. The x-axis represents the normalized buoyancy anomaly, quantified as the disparity between buoyancy under warm and ambient conditions, normalized by the maximal buoyancy value observed under ambient conditions for each respective month.

An overarching trend is evident: the influence of external heating during the Summer and Winter solstices on zonal wind anomalies surpasses that observed during the spring and autumn equinoxes. External heating in the Northern Hemisphere (NH) exerts a positive influence on zonal wind velocity from the equator to the mid-latitudes, whereas it yields a negative effect in the Southern Hemisphere (SH). Likewise, during the winter solstice, this effect is reversed, with the NH and SH experiencing opposing shifts in zonal wind velocity.

Figure 4 demonstrates that radiative forcing during the summer and winter solstices induces northward and southward shifts in atmospheric circulation, respectively. In contrast, during the autumn and spring equinoxes, a weak equatorward displacement of large-scale circulations is observed. Concerning the eddy heat flux, all scenarios of ra-
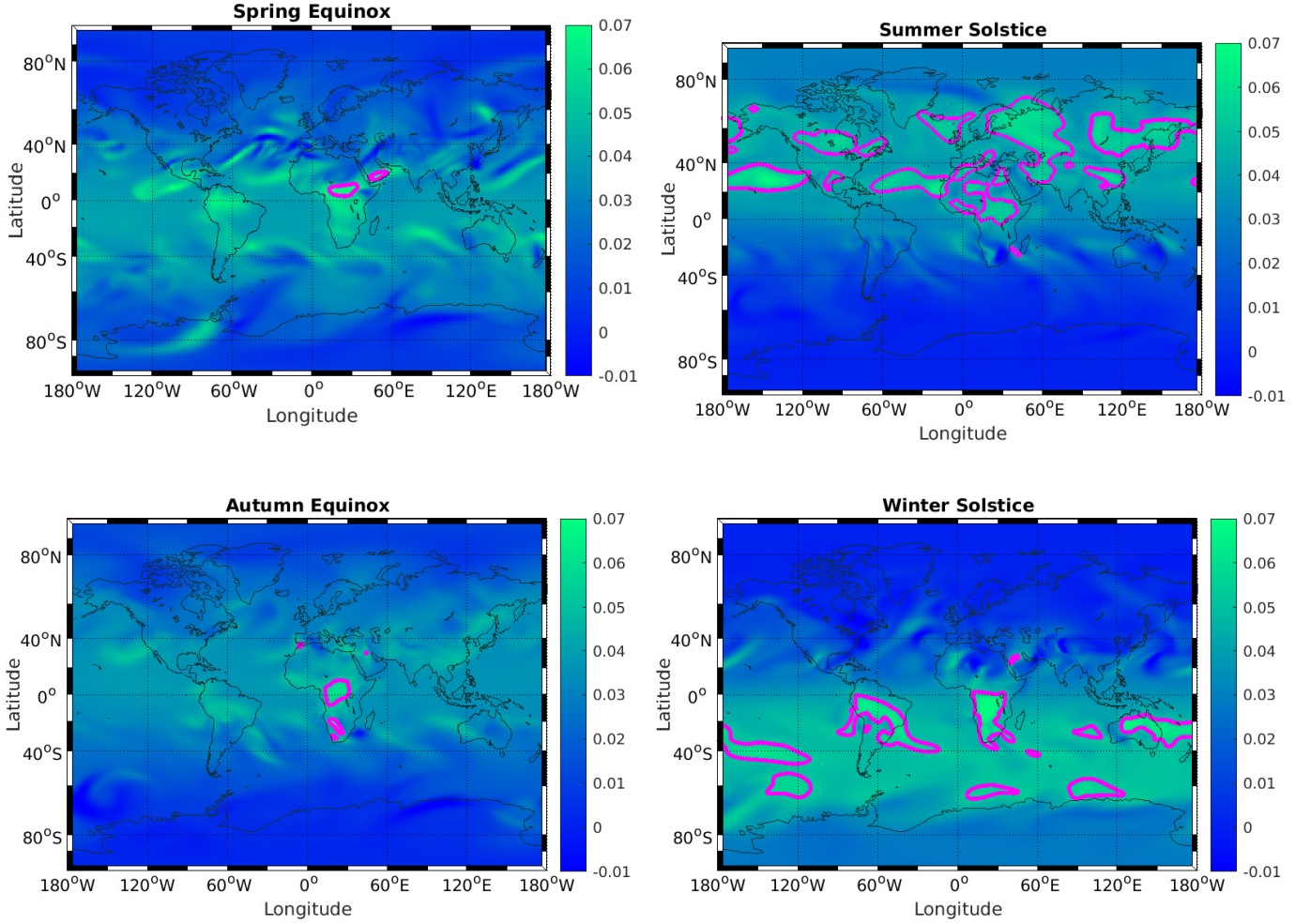
23

Figure 6. The figure presents a spatial distribution comparison of total energy anomalies in the lower layer across four distinct seasonal periods: the Spring Equinox, Summer Solstice, Autumn Equinox, and Winter Solstice. This analysis captures energy perturbations attributed to external heating influences. Thick magenta contour lines highlight regions with energy anomalies greater than 75% of the maximum value observed under unforced conditions for each respective month. The x-axis represents the normalized energy anomaly, quantified as the disparity between energy under warm and ambient conditions, normalized by the maximal energy value observed under unforced conditions for each respective month.

diative forcing exhibit a poleward eddy heat flux in both the NH and SH. The spatial distributions of buoyancy and energy perturbations in the lower troposphere, calculated using Equation C.3 and influenced by external radiative forcings, are shown in Figures 5 and 6. These perturbations exhibit a latitudinal shift from higher to lower latitudes as the seasonal cycle progresses from the Summer Solstice, through the Autumn Equinox and Spring Equinox, to the Winter Solstice. Additionally, the contrast in thermal radiative forcing between land and sea in the Northern Hemisphere induces an asymmetric response in the potential temperature anomalies, particularly between the summer and winter solstices.

Radiative forcing during the Summer and Winter Solstices contributes to the occurrence of prolonged heatwaves, both over land and oceanic regions. Regions exhibiting

significant temperature and energy anomalies, delineated by thick magenta contour lines, such as Australia during the Winter Solstice or Central Asia during the Summer Solstice, represent critical zones highly susceptible to extreme heatwaves. This assertion is substantiated by several observational studies (Fallah and Rostami, 2024; Fallah et al., 2024). These poleward eddy heat fluxes predominate within the latitudinal bands of 40° to 80° in the Northern Hemisphere and -40° to -80° in the Southern Hemisphere.

4   Conclusion

We introduced the dynamical core of Aeolus 2.0, an atmospheric model of intermediate complexity, and employed it to explore the impacts of increased radiative forcing on atmospheric circulation, zonal wind dynamics, and extreme heatwaves. The proposed moist-convective Thermal Rotating Shallow Water (mcTRSW) model aims to address the limitations of traditional shallow water models. The moist-convective scheme represents thermodynamic processes by including latent heat release, condensation, downdrafts, cooling effects, and sea surface evaporation. The model also incorporates insolation, radiative fluxes, and precipitable water, enabling the simulation of moisture-related dynamics, extreme rainfall, and heatwaves. By adopting a multi-layer approach, the model can simulate barotropic and baroclinic processes. The use of spin-weighted spherical harmonics enhances numerical stability and ensures precision by eliminating singularities at the poles, making Aeolus 2.0 suitable for global-scale simulations. The model is designed to bridge the gap between idealized shallow water models and complex three-dimensional general circulation models (GCMs).

Utilizing Aeolus 2.0, we demonstrate how increased radiative forcing affects zonal wind velocities in subtropical and polar regions. This study clarifies the relationship between external heating, zonal wind dynamics, and the spatial distribution of potential temperature patterns in the Earth's atmosphere during equinoxes and solstices. Key findings suggest that augmented radiative forcing induces seasonally dependent meridional temperature gradients, yielding asymmetric effects across hemispheres and subsequently impacting zonal wind velocity. Particularly, during Summer and Winter solstices, this phenomenon results in:

- An increase in zonal wind velocity in the subtropics of the affected hemisphere.

- A decrease in zonal wind velocity in the opposite hemisphere.
- A reduction in zonal wind velocity of the polar cyclone within the same hemisphere.

Our study reveals robust seasonal shifts in atmospheric circulation induced by increased radiative forcing. During summer and winter solstices, pronounced northward and southward shifts occur, respectively, while weaker equatorward displacements are observed during autumn and spring equinoxes. Additionally, consistent poleward eddy heat fluxes across hemispheres indicate a strong response to external heating. Radiative forcing during the Summer and Winter Solstices significantly contributes to the occurrence of prolonged heatwaves over both land and oceanic regions, surpassing the impact observed during the Spring and Autumn Equinoxes.

These findings underscore the significance of external heating as a major driver of atmospheric circulation patterns. Understanding these dynamics is vital for comprehending and potentially mitigating the impacts of contemporary climate change. Moving forward, continued research efforts, such as investigating Arctic/Antarctic amplifications, are essential to further elucidate the interactions between external forcings, atmospheric dynamics, and precipitation patterns.

5   Open Research Section

Aeolus 2.0 has been published as an open-source software package (Rostami et al., 2024a) and is available on Zenodo https://doi.org/10.5281/zenodo.13899262. The most recent iteration of the model, installation procedures, and initialization tailored to specific scientific endeavors can be found in the same location.

A Derivation of the Multi-Layer Thermal Rotating Shallow Water (TRSW) Model

In the pursuit of a comprehensive exposition of the dynamical core, we herein revisit the derivation of the model as proposed by Rostami et al. (2022). Within the framework of the "dry" multi-layer TRSW model, incorporating density variations entails considering the variation of potential temperature. This endeavor commences with the vertical integration of atmospheric primitive equations, utilizing pseudo-height isobaric vertical coordinates Hoskins and Bretherton (1972) in Cartesian coordinates (x, y, z):

$$\frac{\partial \boldsymbol{v}_h}{\partial t} + \mathcal{V} \cdot \boldsymbol{\nabla} \boldsymbol{v}_h + f \hat{\boldsymbol{z}} \times \boldsymbol{v}_h = -\boldsymbol{\nabla}_h \Phi, \tag{A.1a}$$

$$\frac{\partial \Phi}{\partial z} = g \frac{\theta}{\theta_s}, \tag{A.1b}$$

$$\boldsymbol{\nabla}_h \cdot \boldsymbol{v}_h + \frac{\partial w}{\partial z} = 0, \tag{A.1c}$$

$$\frac{\partial \theta}{\partial t} + \boldsymbol{v}_h \cdot \boldsymbol{\nabla}_h \theta + w \frac{\partial \theta}{\partial z} = 0. \tag{A.1d}$$

These equations delineate the horizontal momentum (A.1a), the hydrostatic relation (A.1b), the incompressibility (A.1c), and the conservation of potential temperature (A.1d), respectively, from top to bottom. Here, $\mathcal{V} = (u, v, w)$ represents the 3D velocity field, $\boldsymbol{v}_h = (u, v)$ denotes its horizontal component, Φ represents the geopotential, $\boldsymbol{\nabla}$ and $\boldsymbol{\nabla}_h$ are the three- and two-dimensional gradient operators, respectively. Additionally, θ is the potential temperature of the fluid with a reference potential temperature θ_s at sea level, and g and $\hat{\boldsymbol{z}}$ correspond to gravity acceleration and the unit vector in the vertical direction, respectively.

Considering an m-layer configuration, we employ the standard procedure of vertically averaging (A.1a) between the pseudo-height surfaces $z_i(x, y, t)$ and $z_{i+1}(x, y, t)$. This involves making the mean-field (columnar motion) approximation, enabling the separation of averages of products into products of averages. In this context, the layer enumeration proceeds from bottom to top, such that $z_0 < z_1 < ... < z_m$, where $h_i = z_i - z_{i-1}$ denotes the layer thickness. Here, m represents the number of layers, and z_0 signifies the lowermost material surface. Consequently, the derived "master" equation is expressed

as follows:

$$(z_i - z_{i-1}) \left(\frac{\partial \boldsymbol{v}_i}{\partial t} + (\boldsymbol{v}_i \cdot \boldsymbol{\nabla}) \boldsymbol{v}_i + f \hat{\boldsymbol{z}} \times \boldsymbol{v_i} \right) = -\boldsymbol{\nabla} \left(\frac{1}{2} \frac{g \bar{\theta}_i}{\theta_s} (z_i - z_{i-1})^2 + \Phi(z_{i-1}) h_i \right)$$
$$+ \Phi(z_i) \boldsymbol{\nabla} z_i - \Phi(z_{i-1}) \boldsymbol{\nabla} z_{i-1}. \tag{A.2}$$

After the averaging process, the subscript "h" is omitted. Velocity $\boldsymbol{v}$ and $\boldsymbol{\nabla}$ are understood as two-dimensional vectors henceforth. The Lagrangian derivative $d_i/dt = \partial/\partial t + \boldsymbol{v}_i \cdot \boldsymbol{\nabla}$ will be employed. In the atmospheric case, the layer-averaged buoyancy variable is defined as $b_i = g\bar{\theta}_i/\theta_s$, where $\bar{\theta}_i$ represents the layer-averaged potential temperature. From the hydrostatic equation (A.1b), we derive:

$$\Phi(z_i) = \Phi(z_{i-1}) + h_i b_i = \Phi(z_0) + \sum_{j=1}^{i} \frac{g \bar{\theta}_j}{\theta_s} h_j = \Phi(z_0) + \sum_{j=1}^{i} h_j b_j. \tag{A.3}$$

Here, j represents the index in the sigma notation. For each layer of the TRSW model, the corresponding vertically integrated equations can be expressed as:

$$\frac{d_i \boldsymbol{v}_i}{dt} + f \hat{\boldsymbol{z}} \times \boldsymbol{v}_i = b_i \boldsymbol{\nabla} z_i + \frac{1}{2} h_i \boldsymbol{\nabla} b_i - \boldsymbol{\nabla} \left(\Phi(z_0) + \sum_{j=1}^{i} h_j b_j \right), \tag{A.4a}$$

$$\frac{\partial h_i}{\partial t} + \boldsymbol{\nabla}(h_i \boldsymbol{v}_i) = 0, \tag{A.4b}$$

$$\frac{d_i b_i}{dt} = 0. \tag{A.4c}$$

In the atmosphere, potential temperature is expected to increase with (pseudo -) height, signifying that the layer with the highest b is positioned at the top. This is in contrast to the oceanic model where the layer ordering is inverted. The pseudo-height, a function of pressure, serves as a modified pressure coordinate, allowing for variation at the ground (the lowermost material surface, z_0) as a free surface. A "flat top" boundary condition with constant pressure, and hence constant z, is typically imposed at the uppermost material surface, roughly interpreted as the tropopause. To derive a two-layer TRSW reduction of the atmospheric primitive equations, we introduce the layer thicknesses: $h_1 = z_1 - z_0$ and $h_2 = z_2 - z_1$. The boundary conditions are $\Phi \mid_{z_0} =$ constant and $\boldsymbol{\nabla} z_2 = 0$. Substituting the pseudo-height surfaces in equation (A.4a) with thicknesses and considering the boundary conditions, the momentum equations can be

simplified to the following final form:

$$\frac{d_1 \boldsymbol{v}_1}{dt} + f\hat{\boldsymbol{z}} \times \boldsymbol{v}_1 = -\frac{1}{2}h_1\boldsymbol{\nabla}b_1 - b_1\boldsymbol{\nabla}(h_1 + h_2), \tag{A.5a}$$

$$\frac{d_2 \boldsymbol{v}_2}{dt} + f\hat{\boldsymbol{z}} \times \boldsymbol{v}_2 = \frac{1}{2}h_2\boldsymbol{\nabla}b_2 - \boldsymbol{\nabla}(h_1 b_1 + h_2 b_2). \tag{A.5b}$$

B Thermo-Quasi-Geostrophic Balance Relations for the Barotropic and Baro-clinic State

To attain the thermo-quasi-geostrophic (TQG) limit of the "dry" TRSW model in the barotropic case without topography, we employ the following scaling:

$$(u, v) \sim U, \quad (x, y) \sim L, \quad h \sim H_0(1 + \lambda\eta), \quad b \sim B(1 + 2\lambda b'), \quad f \sim f_0(1 + \lambda y), \tag{B.1}$$

where λ is a small nondimensional parameter, and η is a deviation from thickness at rest H_0. The nondimensional momentum equation, after ignoring higher-order terms in the right-hand side, is:

$$Ro\frac{d\boldsymbol{v}}{dt} + (1 + \lambda y)\hat{\boldsymbol{z}} \times \boldsymbol{v} = -\frac{Bu\lambda}{Ro}\boldsymbol{\nabla}(\eta + b'), \tag{B.2}$$

where $Bu = BH/f_0^2 L^2$ is the Burger number. In line with the standard quasi-geostrophic regime, we assume that deviations of thickness and buoyancy from their mean values are small, e.g., of the same order as the Rossby number $Ro = U/f_0 L = \lambda$. If we assume $Bu \approx 1$, then equation B.2 simplifies to:

$$\hat{\boldsymbol{z}} \times \boldsymbol{v} = -\boldsymbol{\nabla}(\eta + b') = \boldsymbol{\nabla}\psi, \tag{B.3}$$

where $\psi = \eta + b'$ is the geostrophic streamfunction.

By a similar scaling, we can derive the corresponding nondimensional momentum equations of a two-layer TRSW model that can be deduced from (A.5). We consider a constant geopotential at the lower boundary. Using the following scaling, we represent

thicknesses and buoyancy fields as:

$$(u_{1,2}, v_{1,2}) \sim U, \quad (x,y) \sim L, \quad h_{1,2} \sim H_0(\delta_{1,2} + \lambda\eta_{1,2}), \quad b_{1,2} \sim B_0(B_{1,2} + \lambda b'_{1,2}), \quad f \sim f_0,$$

$$\text{(B.4)}$$

where $\delta_{1,2} = H_{1,2}/H_0$ is the nondimensional thickness, $\eta_{1,2}$ is the deviation of thicknesses from $\delta_{1,2}$, $b'_{1,2}$ is buoyancy perturbations, and indices $1, 2$ represent the lower and upper layers, respectively. This scaling yields:

$$Ro\frac{d\boldsymbol{v_1}}{dt} + \sin(\phi)\hat{\boldsymbol{z}} \times \boldsymbol{v_1} = -\frac{Bu\lambda}{Ro}\left(\frac{\delta_1}{2}\boldsymbol{\nabla}b'_1 + B_1\boldsymbol{\nabla}(\eta_1 + \eta_2)\right), \tag{B.5a}$$

$$Ro\frac{d\boldsymbol{v_2}}{dt} + \sin(\phi)\hat{\boldsymbol{z}} \times \boldsymbol{v_2} = -\frac{Bu\lambda}{Ro}\left(\delta_1\boldsymbol{\nabla}b'_1 + \frac{\delta_2}{2}\boldsymbol{\nabla}b'_2 + B_1\boldsymbol{\nabla}\eta_1 + B_2\boldsymbol{\nabla}\eta_2\right), \tag{B.5b}$$

where ϕ is the latitude. Thus, the thermo-geostrophic balance relations between velocity and gradients of pressure and buoyancy perturbations are:

$$\sin(\phi)\hat{\boldsymbol{z}} \times \boldsymbol{v_1} = \frac{\delta_1}{2}\boldsymbol{\nabla}b'_1 + B_1\boldsymbol{\nabla}(\eta_1 + \eta_2), \tag{B.6a}$$

$$\sin(\phi)\hat{\boldsymbol{z}} \times \boldsymbol{v_2} = \delta_1\boldsymbol{\nabla}b'_1 + \frac{\delta_2}{2}\boldsymbol{\nabla}b'_2 + B_1\boldsymbol{\nabla}\eta_1 + B_2\boldsymbol{\nabla}\eta_2. \tag{B.6b}$$

C   Hamiltonian Structure of the TRSW Model

Building upon Ripa's work on inhomogeneous layered models (Ripa, 1993), we formulate the Hamiltonian structure for a two-layer TRSW model in a "dry" environment, considering the influence of bottom topography. Unlike classical Poisson bracket, the generalized Poisson brackets may be degenerate. If a system is Hamiltonian, then the evolution equations governing the field variables φ^a can be expressed utilizing the generalized Hamiltonian structures as follows:

$$\partial_t \varphi^a = \{\varphi^a, \mathscr{H}\} = \mathbb{J}^{ab}\frac{\delta\mathscr{H}}{\delta\varphi^b}. \tag{C.1}$$

Here, $\mathscr{H}$ represents the Hamiltonian, and $\mathbb{J}$ denotes the Poisson tensor, which must possess skew-adjoint properties and satisfy the Jacobi identity. The Poisson bracket

between two functionals is given in terms of $\mathbb{J}$ through the volume integral:

$$\{\mathscr{F},\mathscr{G}\}= \int_{\mathscr{D}} d^2x \frac{\delta\mathscr{F}}{\delta\varphi^a}\mathbb{J}^{ab}\frac{\delta\mathscr{G}}{\delta\varphi^b}. \tag{C.2}$$

In the above equation, with summation over repeated indices, $\mathscr{F}$ and $\mathscr{G}$ represent functionals, $\delta\mathscr{F}/\delta\varphi^a$ and $\delta\mathscr{G}/\delta\varphi^b$ denote the functional derivatives of $\mathscr{F}$ and $\mathscr{G}$ with respect to any particular representation of the state variables φ^a. This representation is defined by $\mathscr{F}(\varphi^a+\varepsilon\mu^a) = \mathscr{F}(\varphi^a)+\varepsilon \int d^2x\,(\delta\mathscr{F}/\delta\varphi^a)\mu^a+\mathcal{O}(\varepsilon^2)$, where $\mu^a(\mathbf{x})$ is arbitrary and $\varepsilon \to 0$. The integral (C.1) is performed over the domain $\mathscr{D}$. According to the Jacobi identity, for any three functionals, $\mathscr{F},\mathscr{G}$, and $\mathscr{K}$, $\{\{\mathscr{F},\mathscr{G}\},\mathscr{K}\}+\{\{\mathscr{G},\mathscr{K}\},\mathscr{F}\}+\{\{\mathscr{K},\mathscr{F}\},\mathscr{G}\}= 0$.

A suitable Hamiltonian, serving as a comprehensive measure of the total energy in the system described by Equation (2.1), encompassing both kinetic energy and gravitational potential energy, can be defined as:

$$\mathscr{H} = \int_{\mathscr{D}} d^2x \left[h_1\left(\frac{1}{2}\boldsymbol{v}_1^2 + \tilde{h}_1 b_1\right) + h_2\left(\frac{1}{2}\boldsymbol{v}_2^2 + \tilde{h}_2 b_2\right)\right]. \tag{C.3}$$

The functional derivatives of the Hamiltonian $\mathscr{H}$ are:

$$\frac{\delta\mathscr{H}}{\delta\boldsymbol{v}_k} = h_k\boldsymbol{v}_k, \quad \frac{\delta\mathscr{H}}{\delta h_k} = \xi_k, \quad \frac{\delta\mathscr{H}}{\delta b_k} = h_k\tilde{h}_k. \tag{C.4}$$

Here, $\xi_i = \tilde{p}_i + (1/2)\boldsymbol{v}_i^2$ represents the Bernoulli head in each layer. It is important to note that, in general, $\partial\tilde{h}_k/\partial h_k$ does not vanish when calculating $\delta\mathscr{H}/\delta h_k$. The total mechanical energy of the system, as defined in Equation (C.3), remains conserved, ensuring the boundedness of the system's free evolution. The term $d^2x\,(1/2)h_i\boldsymbol{v}_i^2$ represents the kinetic energy associated with an elementary fluid column in the ith layer, calculated under the Boussinesq approximation. Furthermore, the height of the elementary column above the reference level $z = 0$ in the ith layer is denoted as $\tilde{h}_i$, and its absolute potential energy is given by $d^2x\,h_i\tilde{h}_i b_i$. This conservation applies to the sum of kinetic energy and potential energy of the active layers, relative to them being filled with stable stratified layers with potential temperatures $\theta_2 > \theta_1$. The definiteness of $\mathscr{H}$ indicates that the solutions of the fully nonlinear equations cannot undergo an "explosion" from a state of rest, ensuring that the free evolution of the system remains bounded. By considering

the layer-wise potential vorticity as:

$$\mathbb{Q}_i = \frac{f + \partial_x v_i - \partial_y u_i}{h_i}, \quad i = 1, 2, \tag{C.5}$$

we can rewrite the equations describing the evolution of velocity, (2.1b) and (2.1c), as:

$$\partial_t u_i - \mathbb{Q}_i h_i v_i + \partial_x \xi_i = \tilde{h}_i \partial_x b_i, \quad i = 1, 2, \tag{C.6a}$$

$$\partial_t v_i + \mathbb{Q}_i h_i u_i + \partial_y \xi_i = \tilde{h}_i \partial_y b_i, \quad i = 1, 2. \tag{C.6b}$$

From equations (2.1) and (C.5), we can infer that the potential vorticity follows the following equation and is not conserved:

$$\partial_t \mathbb{Q}_i + \boldsymbol{v}_i \cdot \boldsymbol{\nabla} \mathbb{Q}_i = h_i^{-1} \mathcal{J}(\tilde{h}_i, b_i), \quad i = 1, 2, \tag{C.7}$$

where the operator $\mathcal{J}(f, g) = \partial_x f \partial_y g - \partial_y f \partial_x g$ is the Jacobian of the two functions. When the condition $\boldsymbol{\nabla} b_i = 0$ holds, equation (C.7) represents the conservation of potential vorticity ($\partial_t \mathbb{Q}_i + \boldsymbol{v}_i \cdot \boldsymbol{\nabla} \mathbb{Q}_i = 0$), indicating that the potential vorticity is conserved as the fluid elements move in the classical RSW equations. If density gradients are present within the layer, potential vorticity $\mathbb{Q}_i$ does not remain conserved. If $\nabla \tilde{h}_i$ is collinear with ∇b_i, it indicates a symmetry in the system that leads to the conservation of certain quantities, often referred to as Casimirs or $\mathbb{Q}$, throughout the system's evolution. Casimirs are functionals of the phase space variables that remain constant along the system's trajectories. This conservation ensures the stability and boundedness of the system. Equations (2.1) may be written in non-canonical Hamiltonian form as:

$$\partial_t(\varphi) = \mathbb{J} \begin{pmatrix} \mathbb{M}_1 \\ \\ \mathbb{M}_2 \end{pmatrix}, \tag{C.8}$$

where $(\varphi) = (b_1, h_1, u_1, v_1, b_2, h_2, u_2, v_2)^T$ represent the phase space, comprising the variables b_i, h_i, u_i, v_i with $i = 1, 2$, in the domain $\mathscr{D}$. Notably, the system exhibits no normal flux across the domain. The matrix $\mathbb{O}$ within the Poisson tensor is a null matrix of size 4×4. The Poisson tensor itself takes a block diagonal form, and the matrices $\mathbb{M}_i$ are

defined as follows:

$$\mathbb{J} = \begin{pmatrix} \mathbb{J}_1 & \mathbb{O} \\ \mathbb{O} & \mathbb{J}_2 \end{pmatrix}, \quad \mathbb{J}_i = \begin{pmatrix} 0 & 0 & -h_i^{-1}\partial_x b_i & -h_i^{-1}\partial_y b_i \\ 0 & 0 & -\partial_x & -\partial_y \\ h_i^{-1}\partial_x b_i & -\partial_x & 0 & \mathbb{Q}_i \\ h_i^{-1}\partial_y b_i & -\partial_y & -\mathbb{Q}_i & 0 \end{pmatrix}, \quad i = 1, 2, \qquad \text{(C.9a)}$$

$$\mathbb{M}_i = \begin{pmatrix} h_i \tilde{h}_i \\ \xi_i \\ h_i u_i \\ h_i v_i \end{pmatrix}, \quad i = 1, 2. \qquad \text{(C.9b)}$$

Although the matrix $\mathbb{J}$ in Equation (C.9a) is not inherently antisymmetric, its skew-adjoint property implies that for any pair of admissible functionals of the state, $\mathscr{F}(\varphi)$ and $\mathscr{G}(\varphi)$, the relation $\{\mathscr{F}, \mathscr{G}\} = -\{\mathscr{G}, \mathscr{F}\}$ holds, as shown in equation (C.10). In the case where gradients of potential temperature are absent, the rank of the Poisson tensor (C.9a) is reduced. To clarify, the Poisson bracket (C.2) can be written in the following form:

$$\{\mathscr{F}, \mathscr{G}\} = \int_{\mathscr{D}} d^2x \left[h^{-1}\boldsymbol{\nabla}b \left(\frac{\delta\mathscr{F}}{\delta\boldsymbol{v}}\frac{\delta\mathscr{G}}{\delta b} - \frac{\delta\mathscr{G}}{\delta\boldsymbol{v}}\frac{\delta\mathscr{F}}{\delta b} \right) + \boldsymbol{\nabla}\cdot\left(\frac{\delta\mathscr{F}}{\delta\boldsymbol{v}} \right)\frac{\delta\mathscr{G}}{\delta h} - \boldsymbol{\nabla}\cdot\left(\frac{\delta\mathscr{G}}{\delta\boldsymbol{v}} \right)\frac{\delta\mathscr{F}}{\delta h} + \mathbb{Q}\left(\frac{\delta\mathscr{F}}{\delta u}\frac{\delta\mathscr{G}}{\delta v} \right. \right.$$
$$\text{(C.10)}$$

The inclusion of the gradient operator in (C.9a) implies that for the Poisson bracket to exhibit antisymmetry, the admissible functionals must satisfy the condition:

$$\boldsymbol{n} \cdot \frac{\delta\mathscr{F}}{\delta\boldsymbol{v}_i} = 0, \quad \mathbf{x} \in \partial\mathscr{D}, \quad i = 1, 2. \qquad \text{(C.11)}$$

This condition specifies that the normal component of the functional derivative of $\mathscr{F}$ with respect to $\boldsymbol{v}_i$ must be zero at the boundary $\partial\mathscr{D}$ for both the $i = 1$ and $i = 2$ layers.

The Poisson bracket between an arbitrary functional of state, denoted as $\mathscr{F}$, and the Hamiltonian, denoted as $\mathscr{H}$, can be straightforwardly determined using the following

expression:

$$\{\mathscr{F}, \mathscr{H}\} = \int_{\mathscr{D}} d^2x \left[\frac{\delta \mathscr{F}}{\delta \boldsymbol{v}} \cdot \partial_t \boldsymbol{v} + \frac{\delta \mathscr{F}}{\delta h} \partial_t h + \frac{\delta \mathscr{F}}{\delta b} \partial_t b \right]. \tag{C.12}$$

This expression captures the contribution of the rate of change of $\mathscr{F}$ that arises from its dependence on the state variables $\varphi^a(\mathbf{x}, t)$, rather than an explicit dependence on time t. It accounts for the effects of the time evolution of the variables $\boldsymbol{v}$, h, and b on $\mathscr{F}$.

In the system, in addition to the total mechanical energy, an infinite number of conserved Casimirs exist. These Casimirs, represented as $\mathscr{C}(\varphi)$, are associated with arbitrary functions of potential temperature rather than potential vorticity. As functionals of the system's state, the gradients of these Casimirs satisfy the condition $\mathbb{J}^{ab} \left(\delta \mathscr{C} / \delta \varphi^b \right) = 0$, indicating that their functional gradients with respect to the variables φ^b lie within the null space of the Poisson tensor $\mathbb{J}$, which is known to be singular (Morrison, 1998; Shepherd, 1990). This property ensures the invariance of the Casimirs during the system's evolution. An equivalent condition stated in terms of the Poisson bracket is $\{\mathscr{C}, \mathscr{F}\} = 0$ for all functionals $\mathscr{F}$. This implies that the Poisson bracket between any pair of Casimirs and functionals vanishes, further reinforcing the conservation of Casimirs as the system evolves. The Casimir functionals for equations (C.9a) and (C.10) can be written as follows:

$$\mathscr{C}(\varphi) = \int_{\mathscr{D}} d^2x \, h_i \left[\mathbb{Q}_i F(b_i) + G(b_i) \right], \quad i = 1, 2, \tag{C.13}$$

where F_i and G_i are arbitrary functions. These Casimir functionals capture the conservation principles associated with potential temperature functions in the system. The necessary boundary conditions for the Casimirs are $\hat{n} \cdot \boldsymbol{v}_i = 0$ and $\nabla b_i \times \hat{n} = 0$ on the boundary $\partial \mathscr{D}$. These conditions ensure that the Casimirs remain constant and unaffected by flow or temperature variations at the boundaries of the system.

References

Arnold, V. I., 1978. Mathematical Methods of Classical Mechanics. Springer, New York.

Beron-Vera, F., 2021. Multilayer shallow–water model with stratification and shear. Revista Mexicana de Física 67 (3), 351–364.
URL https://doi.org/10.31349/revmexfis.67.351

Betts, A., Miller, M., 1986. A new convective adjustement scheme. Part II: Single columns tests using GATE wave, BOMEX, ATEX and arctic air-mass data sets. Quarterly Journal of the Royal Meteorological Society 112, 693–762.

Bouchut, F., Lambaerts, J., Lapeyre, G., Zeitlin, V., 2009. Fronts and nonlinear waves in a simplified shallow–water model of the atmosphere with moisture and convection. Physics of Fluids 21 (11), 116604.
URL https://doi.org/10.1063/1.3265970

Burns, K. J., Vasil, G. M., Oishi, J. S., Lecoanet, D., Brown, B. P., Apr 2020. Dedalus: A flexible framework for numerical simulations with spectral methods. Physical Review Research 2, 023068.
URL https://link.aps.org/doi/10.1103/PhysRevResearch.2.023068

Cao, Y., Kurganov, A., Liu, Y., Zeitlin, V., 2023. Flux globalization based well-balanced path-conservative central-upwind scheme for two-layer thermal rotating shallow water equations. Journal of Computational Physics 474, 111790.
URL https://www.sciencedirect.com/science/article/pii/S0021999124005217

Cartwright, D., 1978. Oceanic tides. The International Hydrographic Review.

Fallah, B., Didovets, I., Rostami, M., Hamidi, M., 2024. Climate change impacts on Central Asia: Trends, extremes and future projections. International Journal of Climatology 44 (10), 3191–3213.
URL https://rmets.onlinelibrary.wiley.com/doi/abs/10.1002/joc.8519

Fallah, B., Rostami, M., 2024. Exploring the impact of the recent global warming on extreme weather events in Central Asia using the counterfactual climate data ATTRICI v1.1. Climatic Change 177 (5), 80.
URL https://doi.org/10.1007/s10584-024-03743-0

Francis, J., Skific, N., 2015. Evidence linking rapid Arctic warming to mid-latitude weather patterns. Philosophical Transactions of the Royal Society A: Mathematical,

Physical and Engineering Sciences 373 (2045), 20140170.

URL https://royalsocietypublishing.org/doi/abs/10.1098/rsta.2014.0170

Francis, J. A., Vavrus, S. J., 2015. Evidence for a wavier jet stream in response to rapid Arctic warming. Environmental Research Letters 10 (1), 014005.

URL https://dx.doi.org/10.1088/1748-9326/10/1/014005

Gill, A., 1980. Some simple solutions for heat-induced tropical circulation. Quarterly Journal of the Royal Meteorological Society 106 (449), 447–462.

URL https://doi.org/10.1002/qj.49710644905

Holm, D. D., Luesink, E., Pan, W., 2021. Stochastic mesoscale circulation dynamics in the thermal ocean. Physics of Fluids 33 (4).

URL https://doi.org/10.1063/5.0040026

Holm, D. D., Marsden, J. E., Ratiu, T. S., Weinstein, A. D., 1985. Nonlinear stability of fluid and plasma equilibria. Physics Reports 123, 1–116.

Hoskins, B. J., Bretherton, F. P., 1972. Atmospheric frontogenesis models: Mathematical formulation and solution. Journal of the Atmospheric Sciences 29 (1), 11–37.

URL http://dx.doi.org/10.1175/1520-0469(1972)029<0011:AFMMFA>2.0.CO;2

Iacono, M. J., Mlawer, E. J., Clough, S. A., Morcrette, J.-J., 2000. Impact of an improved longwave radiation model, RRTM, on the energy budget and thermodynamic properties of the NCAR community climate model, CCM3. Journal of Geophysical Research: Atmospheres 105 (D11), 14873–14890.

URL https://doi.org/10.1029/2000JD900091

Kurganov, A., Liu, Y., Zeitlin, V., 2020. Moist-convective thermal rotating shallow water model. Physics of Fluids 32 (6), 066601.

URL https://doi.org/10.1063/5.0007757

Kurganov, A., Liu, Y., Zeitlin, V., 2021. Interaction of tropical cyclone-like vortices with sea-surface temperature anomalies and topography in a simple shallow-water atmospheric model. Physics of Fluids 33 (10), 106606.

URL https://doi.org/10.1063/5.0064481

Lahaye, N., Zeitlin, V., 2016. Understanding instabilities of tropical cyclones and their evolution with a moist convective rotating shallow–water model. Journal of Atmospheric Sciences 73 (2), 505 – 523.

URL https://doi.org/10.1175/JAS-D-15-0115.1

Lambaerts, J., Lapeyre, G., Zeitlin, V., 2011a. Moist versus dry barotropic instability

in a shallow–water model of the atmosphere with moist convection. Journal of Atmospheric Sciences 68, 1234–1252.

URL https://doi.org/10.1175/2011JAS3540.1

Lambaerts, J., Lapeyre, G., Zeitlin, V., 2012. Moist versus dry baroclinic instability in a simplified two–layer atmospheric model with condensation and latent heat release. Journal of Atmospheric Sciences 69, 1405–1426.

URL https://doi.org/10.1175/JAS-D-11-0205.1

Lambaerts, J., Lapeyre, G., Zeitlin, V., Bouchut, F., 2011b. Simplified two–layer models of precipitating atmosphere and their properties. Physics of Fluids 23 (4), 046603.

URL https://doi.org/10.1063/1.3582356

Landau, L. D., Lifshitz, E. M., 1976. Mechanics. Pergamon Press, Oxford.

Lavoie, R. L., 1972. A mesoscale numerical model of lake–effect storms. Journal of Atmospheric Sciences 29 (6), 1025 – 1040.

Lecoanet, D., Vasil, G. M., Burns, K. J., Brown, B. P., Oishi, J. S., 2019. Tensor calculus in spherical coordinates using Jacobi polynomials. Part–II: Implementation and examples. Journal of Computational Physics 3, 100012.

URL https://doi.org/10.1016/j.jcpx.2019.100012

Lupo, A. R., 2021. Atmospheric blocking events: a review. Annals of the New York Academy of Sciences 1504 (1), 5–24.

URL https://nyaspubs.onlinelibrary.wiley.com/doi/abs/10.1111/nyas.14557

Mann, M. E., Rahmstorf, S., Kornhuber, K., Steinman, B. A., Miller, S. K., Petri, S., Coumou, D., 2018. Projected changes in persistent extreme summer weather events: The role of quasi-resonant amplification. Science Advances 4 (10), eaat3272.

URL https://www.science.org/doi/abs/10.1126/sciadv.aat3272

Matsuno, T., 1966. Quasi-geostrophic motions in the equatorial area. Journal of the Meteorological Society of Japan. Ser. II 44 (1), 25–43.

Mattsson, A. E., Rider, W. J., 2015. Artificial viscosity: back to the basics. International Journal for Numerical Methods in Fluids 77 (7), 400–417.

URL https://doi.org/10.1002/fld.3981

Mlawer, E. J., Taubman, S. J., Brown, P. D., Iacono, M. J., Clough, S. A., 1997. Radiative transfer for inhomogeneous atmospheres: RRTM, a validated correlated-k model for the longwave. Journal of Geophysical Research: Atmospheres 102 (D14), 16663–

16682.

URL https://doi.org/10.1029/97JD00237

Moon, W., Kim, B.-M., Yang, G.-H., Wettlaufer, J. S., 2022. Wavier jet streams driven by zonally asymmetric surface thermal forcing. Proceedings of the National Academy of Sciences 119 (38), e2200890119.

URL https://www.pnas.org/doi/abs/10.1073/pnas.2200890119

Morrison, P. J., 1998. Hamiltonian description of the ideal fluid. Review of Modern Physics 70, 467–521.

Pedlosky, J., 1987. Geophysical Fluid Dynamics, 2nd ed. Springer-Verlag, New York.

Penman, H. L., 1948. Natural evaporation from open water, bare soil and grass. Proceedings of the Royal Society of London. Series A, Mathematical and Physical Sciences 193 (1032), 120–145.

URL http://www.jstor.org/stable/98151

Petoukhov, V., Rahmstorf, S., Petri, S., Schellnhuber, H. J., 2013. Quasiresonant amplification of planetary waves and recent Northern Hemisphere weather extremes. Proceedings of the National Academy of Sciences 110 (14), 5336–5341.

URL https://www.pnas.org/doi/abs/10.1073/pnas.1222000110

Proudman, J., 1942. On Laplace's differential equations for the tides. Proceedings of the Royal Society of London. Series A. Mathematical and Physical Sciences 179 (978), 261–288.

Ripa, P., 1993. Conservation laws for primitive equations models with inhomogeneous layers. Geophysical and Astrophysical Fluid Dynamics 70 (1-4), 85–111.

URL https://doi.org/10.1080/03091929308203588

Ripa, P., 1995. On improving a one–layer ocean model with thermodynamics. Journal of Fluid Mechanics 303, 169–201.

URL https://doi.org/10.1017/S0022112095004228

Ripa, P., 1996. Low frequency approximation of a vertically averaged ocean model with thermodynamics. Revista Mexicana de Física 42 (1), 117–135.

Rostami, M., Petri, S., Guimarães, S. O., Fallah, B., 2024a. Open-source stand-alone version of atmospheric model aeolus 2.0 software. Geoscience Data Journal 11 (4), 1086–1093.

URL https://rmets.onlinelibrary.wiley.com/doi/abs/10.1002/gdj3.249

Rostami, M., Severino, L., Petri, S., Hariri, S., 2024b. Dynamics of localized extreme

heatwaves in the mid-latitude atmosphere: A conceptual examination. Atmospheric Science Letters 25 (1), e1188.

URL https://doi.org/10.1002/asl.1188

Rostami, M., Zeitlin, V., 2017. Influence of condensation and latent heat release upon barotropic and baroclinic instabilities of vortices in a rotating shallow water f-plane model. Geophysical & Astrophysical Fluid Dynamics 111 (1), 1–31.

URL https://doi.org/10.1080/03091929.2016.1269897

Rostami, M., Zeitlin, V., 2018. An improved moist-convective rotating shallow-water model and its application to instabilities of hurricane-like vortices. Quarterly Journal of the Royal Meteorological Society 144 (714), 1450–1462.

URL https://doi.org/10.1002/qj.3292

Rostami, M., Zeitlin, V., 2019a. Eastward–moving convection–enhanced modons in shallow water in the equatorial tangent plane. Physics of Fluids 31, 021701.

URL https://doi.org/10.1063/1.5080415

Rostami, M., Zeitlin, V., 2019b. Geostrophic adjustment on the equatorial beta–plane revisited. Physics of Fluids 31 (8), 081702.

URL https://doi.org/10.1063/1.5110441

Rostami, M., Zeitlin, V., 2020. Evolution, propagation and interactions with topography of hurricane–like vortices in a moist–convective rotating shallow–water model. Journal of Fluid Mechanics 902, A24.

URL https://doi.org/10.1017/jfm.2020.567

Rostami, M., Zeitlin, V., 2021. Eastward-moving equatorial modons in moist-convective shallow-water models. Geophysical & Astrophysical Fluid Dynamics 115 (3), 345–367.

URL https://doi.org/10.1080/03091929.2020.1805448

Rostami, M., Zeitlin, V., 2022. Evolution of double-eye wall hurricanes and emergence of complex tripolar end states in moist-convective rotating shallow water model. Physics of Fluids 34 (6), 066602.

URL https://doi.org/10.1063/5.0096554

Rostami, M., Zeitlin, V., Montabone, L., 2018. On the role of spatially inhomogeneous diabatic effects upon the evolution of Mars' annular polar vortex. Icarus 314, 376–388.

URL https://www.sciencedirect.com/science/article/pii/S0019103517306073

Rostami, M., Zeitlin, V., Spiga, A., 2017. On the dynamical nature of Saturn's North

Polar hexagon. Icarus 297, 59–70.

URL https://doi.org/10.1016/j.icarus.2017.06.006

Rostami, M., Zhao, B., Petri, S., 2022. On the genesis and dynamics of Madden–Julian oscillation-like structure formed by equatorial adjustment of localized heating. Quarterly Journal of the Royal Meteorological Society 148 (749), 3788–3813.

URL https://rmets.onlinelibrary.wiley.com/doi/abs/10.1002/qj.4388

Saint-Venant, A. J. C. B., 1871. Théorie du mouvement non permanent des eaux, avec application aux crues des rivières et à l'introduction de marées dans leurs lits. Comptes rendus hebdomadaires des séances de l'Académie des sciences 73, 147–154 and 237–240.

Saint-Venant, A. J. C. B., 1888a. Mémoire sur la perte de force vive d'un fluide aux endroits où sa section d'écoulement augmente brusquement ou rapidement. Mémoires de l'Académie des sciences de l'Institut de France 44, 193–243.

Saint-Venant, A. J. C. B., 1888b. Mémoire sur la prise en considération de la force centrifuge dans le calcul du mouvement des eaux courantes et sur la distinction des torrents et des rivières. Mémoires de l'Académie des sciences de l'Institut de France 44, 245–273.

Salby, M. L., 1989. Deep circulations under simple classes of stratification. Tellus 41 (1), 48–65.

URL https://doi.org/10.3402/tellusa.v41i1.11820

Salmon, R., 1988. Hamiltonian fluid mechanics. Annual Review of Fluid Mechanics 20, 225–256.

Schopf, P. S., Cane, M. A., 1983. On equatorial dynamics, mixed layer physics and sea surface temperature. Journal of Physical Oceanography 13 (6), 917 – 935.

URL https://doi.org/10.1175/1520-0485(1983)013<0917:OEDMLP>2.0.CO;2

Shepherd, T. G., 1990. Symmetries, conservation laws, and Hamiltonian structure in geophysical fluid dynamics. Vol. 32 of Advances in Geophysics. Elsevier, pp. 287–338.

URL https://www.sciencedirect.com/science/article/pii/S006526870860429X

Vasil, G. M., Lecoanet, D., Burns, K. J., Oishi, J. S., Brown, B. P., 2019. Tensor calculus in spherical coordinates using Jacobi polynomials. Part–I: Mathematical analysis and derivations. Journal of Computational Physics 3, 100013.

URL https://doi.org/10.1016/j.jcpx.2019.100013

Von Neumann, J., Richtmyer, R. D., 1950. A Method for the Numerical Calculation of Hydrodynamic Shocks. Journal of Applied Physics 21 (3), 232–237.

URL https://doi.org/10.1063/1.1699639

Warneford, E. S., Dellar, P. J., 2013. The quasi-geostrophic theory of the thermal shallow water equations. Journal of Fluid Mechanics 723, 374–403.

URL https://doi.org/10.1017/jfm.2013.101

Wirangga, R., Mugisidi, D., Sayuti, A. T., Heriyani, O., 2023. The impact of wind speed on the rate of water evaporation in a desalination chamber. Journal of Advanced Research in Fluid Mechanics and Thermal Sciences 106 (1), 39–50.

URL https://semarakilmu.com.my/journals/index.php/fluid_mechanics_thermal_sciences/article/view/2383

Zeitlin, V., 2018. Geophysical Fluid Dynamics: Understanding (almost) Everything with Rotating Shallow Water Models. Oxford University Press, Oxford.

Zerroukat, M., Allen, T., 2015. A moist Boussinesq shallow water equations set for testing atmospheric models. Journal of Computational Physics 290, 55–72.

URL https://doi.org/10.1016/j.jcp.2015.02.011

Zhao, B., Zeitlin, V., Fedorov, A. V., 2021. Equatorial modons in dry and moist-convective shallow-water systems on a rotating sphere. Journal of Fluid Mechanics 916, A8.

URL https://doi.org/10.1017/jfm.2021.159